Resolution of SARS-CoV-2 infection in human lung tissues is driven by extravascular CD163+ monocytes

Devin Kenney[1,2], Aoife K. O'Connell[1,2,4], Anna E. Tseng[1,2,4], Jacquelyn Turcinovic[1,2,3], Meagan L. Sheehan[7,12], Adam D. Nitido[7,12], Paige Montanaro[2,4], Hans P. Gertje[2,4], Maria Ericsson[6], John H. Connor[1,2], Vladimir Vrbanac[7], Nicholas A. Crossland[1,2,4], Christelle Harly[8,9,12]*, Alejandro B. Balazs[7,12]*, and Florian Douam[1,2,12,13] *

[1]Department of Virology, Immunology, and Microbiology, Boston University Chobanian & Avedisian School of Medicine, Boston, MA, USA.

[2] National Emerging Infectious Diseases Laboratories, Boston University, Boston, MA, USA.

[3] Bioinformatics Program, Boston University, Boston, MA, USA.

[4] Department of Pathology and Laboratory Medicine, Boston University Chobanian & Avedisian School of Medicine, Boston, MA, USA.

[6] Electron Microscopy Core Facility, Harvard Medical School, Boston, MA, USA.

[7] Ragon Institute of MGH, MIT and Harvard, Cambridge, MA, USA.

[8] Université de Nantes, INSERM, CNRS, CRCINA, Nantes, France

[9] LabEx IGO 'Immunotherapy, Graft, Oncology', Nantes, France.

[12] These authors contributed equally to the work.

[13] Lead contact

*Correspondence: fdouam@bu.edu; abalazs@mgh.harvard.edu; christelle.harly@inserm.fr.

ABSTRACT

The lung-resident immune mechanisms driving resolution of SARS-CoV-2 infection in humans remain elusive. Using mice co-engrafted with a genetically matched human immune system and fetal lung xenograft (fLX), we mapped the immunological events defining resolution of SARS-CoV-2 infection in human lung tissues. Viral infection is rapidly cleared from fLX following a peak of viral replication. Acute replication results in the emergence of cell subsets enriched in viral RNA, including extravascular inflammatory monocytes (iMO) and macrophage-like T-cells, which dissipate upon infection resolution. iMO display robust antiviral responses, are transcriptomically unique among myeloid lineages, and their emergence associates with the recruitment of circulating CD4+ monocytes. Consistently, mice depleted for human CD4+ cells but not CD3+ T-cells failed to robustly clear infectious viruses and displayed signatures of chronic infection. Our findings uncover the transient differentiation of extravascular iMO from CD4+ monocytes as a major hallmark of SARS-CoV-2 infection resolution and open avenues for unravelling viral and host adaptations defining persistently active SARS-CoV-2 infection.

52 **INTRODUCTION**

53 Coronavirus disease 2019 (COVID-19) is a respiratory disease that has swept the world since its
54 emergence in the Wuhan province of China in late 2019. The etiologic agent of COVID19, the
55 Severe Acute Respiratory Syndrome Coronavirus 2 (SARS-CoV-2) is a plus-sense, enveloped
56 RNA virus that targets the epithelium of the respiratory tract. Infection results in varying severities
57 of COVID-19, with the majority of cases being mild to asymptomatic. The onset of severe disease
58 is associated with aberrant immune responses (e.g. increased pulmonary infiltration of myeloid
59 lineages, exacerbated inflammation, lymphopenia, and "cytokine storm") and severe lung injury
60 (e.g. lung consolidation, diffuse alveolar damage (DAD), and thrombosis) (Boumaza et al., 2021a;
61 Delorey et al., 2021b; Grant et al., 2021; Gubernatorova et al., 2020; Kosyreva et al., 2021;
62 Schultze and Aschenbrenner, 2021; Zhang et al., 2020).

63 Extensive studies, using both human samples and animal models, have been instrumental in
64 unraveling cellular and molecular processes driving severe COVID19 disease (Edahiro et al.,
65 2023; Fan et al., 2022; Ren et al., 2021; Stephenson et al., 2021). However, the immunological
66 mechanisms defining successful resolution of SARS-CoV-2 infection remain elusive. While a
67 recent study identified HLA-B*15 expression and previous coronavirus exposure as a determinant
68 of rapid SARS-CoV-2 clearance and asymptomatic infection, this involved only 17-25% of
69 asymptomatic patients (Augusto et al., 2023). The ability of SARS-CoV-2 to downregulate HLA-
70 B suggests that other important immune mechanisms enabling SARS-CoV-2 clearance may be
71 at play in the human lung (Moriyama et al., 2023; Yoo et al., 2021).

72 Our limited understanding of the human mechanisms driving effective viral clearance largely
73 stems from the lack of appropriate experimental platforms. Only peripheral blood and bronchiolar
74 lavage samples (which prevent access to the lung interstitial compartment) can be accessed from
75 human patients with asymptomatic or mild COVID-19. There are also logistical challenges
76 associated with the capture of early pulmonary immune responses in infected individuals, and/or
77 in the validation of purely correlative findings, as this requires the need to conduct experimental

78 human infection. Though large and small animal models of COVID-19 have been developed, the
79 high-cost and limited reagent availability associated with non-human primate models, and the
80 large divergence between rodent and human immune systems further underscore the need for
81 additional models capable of recapitulating human protective immune responses to SARS-CoV-
82 2 infection.

83 Mice co-engrafted with human fetal lung xenograft (fLX) and a human immune system (HIS)
84 represent a robust platform to uncover human immunological determinants of SARS-CoV-2
85 infection resolution and lung tissue protection from excessive inflammation (Di et al., 2022;
86 Kenney et al., 2022; Sun et al., 2022a). We recently demonstrated that while mice engrafted with
87 fLX are highly susceptible to SARS-CoV-2 infection and lung tissue damage, co-engraftment of
88 fLX and a HIS in a xenorecipient strain supporting enhanced myelopoiesis (i.e., HNFL mouse
89 model) resulted in complete lung tissue protection from both infection and histopathology (Kenney
90 et al., 2022). Infection was cleared as early as day 2 post-virus inoculation, preventing widespread
91 viral replication in tissues. Macrophage antiviral responses were the dominant correlates of rapid
92 viral clearance and limited tissue damage. However, how the human immune system mobilizes
93 and resolves infection upon extensive viral replication within human lung tissues, a context that
94 more likely describes mild cases of SARS-CoV-2 infection, has remained elusive.

95 In this study, we leverage immunodeficient mice engrafted with a human fetal lung xenograft
96 (fLX) and a genetically matched human immune system, fetal liver and thymus (BLT-L mice) to
97 identify human immune determinants and mechanisms, or lack thereof, that drive SARS-CoV-2
98 resolution or persistence in human lung tissues. Consistent with previous reports (Di et al., 2022;
99 Sun et al., 2022a), BLT-L mice were permissive to SARS-CoV-2 infection following direct viral
100 inoculation into the fLX, with infection swiftly resolving following an early viral replication peak at
101 2-days post-inoculation (dpi). Single cell transcriptomic approaches identified extravascular
102 CD163+ inflammatory monocyte (iMO), which were highly enriched in viral RNA, as the primary
103 mediator of antiviral responses preceding viral clearance. Proteomic and cell depletion assays

104 supported a model in which recruitment of circulating CD4+ monocytes into infected fLX, and their
105 subsequent differentiation as iMO, is a defining feature of infection resolution. Abrogation of
106 infection clearance via systemic depletion of CD4+ cells resulted in persistent SARS-CoV-2
107 replication and a remodeling of lung antiviral responses consistent with chronic viral infection.
108 Collectively, our work sheds light on key immunological mechanisms driving SARS-CoV-2
109 resolution in human lung tissues, and provides experimental evidence that monocyte
110 differentiation into extravascular iMO is a critical hallmark of this process. Our study also
111 underscores the potential of the BLT-L mouse model to inform the development of
112 immunotherapies against viral respiratory infections and examine the cause and consequences
113 of chronic SARS-CoV-2 infection on both the virus and the host.
114

115 **RESULTS**

116 **BLT-L mice effectively clear SARS-CoV-2 infection following acute viral replication**

117 Previous work from our laboratory (Kenney et al., 2022) and others (Di et al., 2022; Sun et al.,
118 2022a; Wahl et al., 2019) have shown that immunodeficient mice can successfully be engrafted
119 with human fetal lung xenograft (fLX) independently, or in combination with a human immune
120 system. In this study, we leveraged a previously reported model co-engrafted with fetal liver and
121 thymus as well as with human hematopoietic stem cells (HSC) and fLX (BLT-L mice) (Wahl et al.,
122 2019). Fetal liver and thymus were engrafted under the renal capsule of adult mice (12-16 weeks
123 old) prior to intravenous HSC injection, while a piece of fLX was surgically introduced
124 subcutaneously on one flank of each animal, as described previously (Wahl et al., 2019). To
125 determine the susceptibility of BLT-L mice to SARS-CoV-2 infection and their ability to effectively
126 clear infection, BLT-L mice were inoculated with SARS-CoV-2 (2019-nCoV/USA_WA1/2020) via
127 intra-graft injection. We used a viral dose (10^6 PFU) that we previously established to drive robust
128 fLX infection in an immunodeficient mouse strain not engrafted with a HIS (Kenney et al., 2022).

129 Throughout the course of infection, mice did not display any weight loss (**Fig. 1 A)** or clinical
130 signs of disease such as lethargy or lack of responsiveness (data not shown). fLX were collected
131 at 2, 6, and 12 dpi to assess lung histopathology and viral titers. Immunohistochemistry (IHC) for
132 SARS-CoV-2 S protein revealed evidence of epithelial cell infection in fLX at 2 dpi, while the
133 majority of viral antigen was cleared by 6 dpi and became undetectable by 12 dpi (**Fig.1 B**[a-d]).
134 SARS-CoV-2 S antigen was primarily detected in the cytoplasm of alveolar epithelium
135 morphologically consistent with type II pneumocytes (AT2 cells) and macrophages within alveolar
136 spaces admixed with necrotic cellular debris and bronchiole epithelium, consistent with the
137 primary cell targets of SARS-CoV-2 (**Fig.1 B**[b]). Transmission electron microscopy (TEM) imaging
138 of fLX at 2 dpi substantiated evidence of productive fLX infection, as evidenced by the presence
139 of viral particles in the cytosol of epithelial cells and budding/invagination of virions (**Fig. S1 A-D**).
140 Viral titer quantification in fLX also supported evidence of acute infection at 2 dpi prior to effective
141 resolution (**Fig.1 C**). A significant amount of infectious viral particles could be recovered from fLX
142 at 2 dpi (3.20 ± 2.52 log([PFU/mg of tissue]), followed by a significant and incremental reduction
143 at 6 dpi (0.281 ± 0.688 log[PFU/mg of tissue]) and 12 dpi (0.111 ± 0.293 log[PFU/mg of tissue])
144 (**Fig. 1 C**). No serum neutralizing activity against SARS-CoV-2 was detected at any time point
145 (**Fig. S1 E,F**). The absence of neutralizing humoral responses contributing to infection resolution
146 is consistent with the rapid clearance of infectious viral particles in fLX.
147 Next, we examined histopathological phenotypes associated with active and resolved fLX
148 infection. Interpretation of hematoxylin and eosin (H&E) staining illustrated denuding of
149 pneumocytes, neutrophil infiltration, edema, hemorrhage, thrombosis, and pneumocyte necrosis
150 at 2 dpi (**Fig. 1 B**[e-h]**; S1 G-I**). No major disease phenotypes were observed at 6 and 12 dpi
151 compared to naïve fLX, underscoring that fLX can mount repair mechanisms upon resolution of
152 infection. A previously described semi-quantitative histopathological scoring system (Kenney et
153 al., 2022) provided statistical confirmation for significant lung pathology at 2 dpi, which was no
154 longer apparent at day 6 dpi (**Fig. 1 D**). Collectively, BLT-L fLX recapitulates important hallmarks

155 of acute SARS-CoV-2 infection, including viral replication and histopathological manifestations of
156 disease, prior to effective viral clearance and lung tissue repair.
157

158 **SARS-CoV-2 induces cellular remodeling of fLX upon infection**

159 We performed bulk-RNA sequencing on fLX to identify gene signatures associated with viral
160 clearance. Strikingly, transcriptomic responses at both 2 and 12 dpi were limited and mostly
161 defined by transcript downregulation relative to naïve fLX mRNA expression (150 and 333 genes
162 at 2 dpi and 12 dpi, respectively) (**Fig. S1 J-N**) which is consistent with the ability of SARS-CoV-
163 2 to accelerate the degradation of cytosolic cellular mRNAs (Finkel et al., 2021). At both time
164 points a smaller subset of genes were upregulated (91 and 21 genes at 2 and 12 dpi,
165 respectively); these upregulated genes primarily associated with B cell response/activation
166 *(FCRL1, FCRL5, FCRLA, CR2, BLK, PAX5 and MZB1)* and immunoglobin recombination
167 (*IGHV3-11, IGHV3-51, IGHD, IGHM, IGHJ3, IGHJ4, IGLV1-36, and IGLC5*) (**Fig. S2 K; Data S1**);
168 albeit no neutralizing antibody responses could be detected in infected BLT-L mice at any time
169 point (**Fig. S1 K**). Low to moderate upregulation of genes associated with NF-kb
170 activation/signaling (*IL1A*, *IL1RL1, TLR9, FABP4*) and monocyte/macrophage activation (*FGR*,
171 *CD101, SLC11A1, HBEGF, TREM1, VSIG4, CCL24*) were also observed (**Data S1**).

172 Given that bulk transcriptomic data provided limited insight into significant gene signatures
173 associated with infection resolution, we hypothesized that antiviral and clearance mechanisms
174 are likely to be compartmentalized within specific immune effectors whose contribution cannot be
175 comprehensively captured using bulk approaches. As we previously reported that effective control
176 of SARS-CoV-2 infection in fLX is dependent on the engraftment of a functional human immune
177 system (Kenney et al., 2022), we performed single-cell RNA sequencing (scRNA-seq) on naïve
178 and infected fLX of BLT-L mice to identify critical immune effectors of viral clearance. While the
179 majority of cells detected by scRNA-seq were human, a minor population of mouse cells were
180 detected in fLX and excluded from downstream analysis (**Fig. S2 A-C**). Analysis of the human

181 compartment revealed diverse immune subsets (T cells/Innate lymphoid cells (ILC), B cells,
182 myeloid cells and mast cells) and non-immune cell types (ciliated and non-ciliated epithelial,
183 endothelial, mesenchymal cells and chondrocytes) in both naïve and infected fLX (**Fig. 2 A,B; S2**
184 **D**). Important to note, because our tissue digestion process favors hematopoietic cell recovery
185 compared to non-immune compartments, the relative representation of the different cell types in
186 fLX is likely biased, as asserted by the limited size of the epithelial compartment. Regardless, the
187 relative dynamics of each cell type captured could be examined upon infection.

188 T-cell/ILC frequency dramatically decreased in fLX upon infection (naïve, 66.8%; 2 dpi, 35.3%;
189 12 dpi, 21.8%), which is consistent with evidence that COVID19 can induce lymphoid depletion
190 (**Fig. 2 B,C**). Notably, lymphopenia was not observed in the peripheral blood of BLT-L mice
191 suggesting lymphocyte depletion in fLX was not directly attributed to declining circulating
192 peripheral lymphocytes (**Fig. S2 E)**. In contrast, myeloid (naïve, 9.94%; 2 dpi, 25.3%; 12 dpi,
193 22.2%) and B-cell subsets (naïve, 3.64%; 2 dpi, 5.38%; 12 dpi, 5.31%) relatively expanded upon
194 infection (**Fig. 2 B,C**). The epithelial, endothelial and mesenchymal cell frequencies also
195 increased upon infection, while mast cell, ciliated cell and chondrocyte frequencies decreased
196 (**Fig. 2 B,C**). Interestingly, within clusters, some cell populations (mesenchymal, myeloid, and T
197 cells/ILCs) showed clear segregation by time point (**Fig. 2 B, S2 F**; 2 dpi: red clusters and 12 dpi:
198 blue clusters), suggesting that infection alters the transcriptional state of some cell types or drives
199 development of novel cell subsets. This temporal segregation suggests a two-step tissue
200 remodeling process upon infection likely involving i) early responses to acute viral replication
201 followed by ii) tissue repair mechanisms and potential immune imprinting.

202 Next, we explored the distribution of viral RNA throughout clusters to determine if temporal-
203 specific clusters associated with the presence of viral RNA. Similar to clearance of infectious viral
204 particles (**Fig. 1C**), viral RNA was not detected in fLX at 12 dpi but was detected in several cell
205 clusters at 2 dpi (**Fig. 2D**). While minor yet detectable expression of viral reads were observed in
206 epithelial, endothelial, chondrocyte and B cell lineages (**Fig. 2 D**), mesenchymal subsets exhibited

207 higher levels of viral reads. However, reads were limited and distributed sporadically without
208 significant enrichment within a given cluster (**Fig. 4 E and Fig S3 A**), (including the 2 dpi-specific
209 mesenchymal cluster defined in group B; **Fig. 2 B**), underscoring a lack of association between
210 viral RNA and mesenchymal activation upon SARS-CoV-2 challenge. In contrast, 2 dpi-specific
211 T-cell and myeloid cell groupings (A and C; **Fig. 2B,E**) were strongly enriched in viral RNA,
212 suggesting a contribution of these subpopulations to the resolution of acute infection.

213 Even though minimal viral RNA was detected in the epithelial compartment, we wished to
214 examine if there were transcriptional indicators of current or prior infection of the epithelium. Initial
215 sub-clustering of the epithelial compartment revealed populations of airway basal and secretory
216 cells, alveolar type 1 (AT1) and type 2 (AT2) cells, and serous cells (**Fig. 2F**). Consistent with
217 hallmarks of COVID-19 in humans, we noted a relative reduction of the AT2 compartment at 2 dpi
218 (25.6%) compared to naïve mice (73.1%), which was partially restored at 12 dpi (49.1%) (**Fig. 2**
219 **F,G**). AT2 cells were not enriched in viral RNA and did not exhibit any robust antiviral responses,
220 consistent with evidence that SARS-CoV-2 infection inhibits type I IFN signaling (Chen et al.,
221 2021). However, they displayed previously reported COVID-19 signatures in human patients
222 including downregulation of MHC genes (*HLA-C, HLA-B, and HLA-DPB1)* and *CCL5* (a cytokine
223 associated with immune recruitment during respiratory infection). Elevated expression of
224 mitochondrial transcripts and transcripts associated with ROS-mediated mitochondrial
225 dysfunctions (i.e., LARS2) were observed upon infection and particularly at 12 dpi, suggestive of
226 major cellular and metabolic remodeling in AT2 cells. (**Fig. 2H**). Consistently, increased levels of
227 *SFTPA1* transcripts, a gene associated with AT2 to AT1 transition upon lung damage, was noted
228 at 2 dpi (**Fig. 2H**). An increase in AT1 and airway basal cell frequencies at 2 dpi (9.89% and
229 60.4%, respectively) compared to naïve fLX (5.00% and 19.4%, respectively) suggest the
230 activation of tissue repair processes of the lung epithelium following infection (**Fig. 2G**).

231 Collectively, these data demonstrate that scRNA-seq has the resolution to capture both
232 immune and non-immune cellular remodeling of fLX during acute SARS-CoV-2 infection and can

233 provide insight into the dynamics of immune-mediated viral clearance. Additionally, SARS-CoV-
234 2 infection within fLX of BLT-L mice mimic many hallmarks of human lung infection.
235
236 **Macrophage-like T-cells are enriched in viral RNA and mount robust antiviral signatures**
237 Next, we aimed to identify the specific T-cell subpopulation that was enriched in viral RNA through
238 sub-clustering of the main T cell/ILC clusters. A CD3+ subpopulation clustered very distinctively
239 from other CD3+ T-cell lineages and was highly enriched in viral RNA (Cluster 6; **Fig. 3 A-C**).
240 Cells included in this subpopulation displayed low levels of both *CD4* and *CD8* transcripts (**Fig. 3**
241 **E**), as well as elevated levels of mitochondrial transcripts **(Fig. S3 B,C**). Most notably, this T-cell
242 subset was uniquely defined by the expression of several transcripts known to be enriched in
243 macrophages (*MARCO*, *TIMP1*, *LYZ*), fibroblasts (*MGP*, *CALD1*, *COL1A*), or both (*A2M*, *IFITM3*)
244 but not in T-cells (**Fig. 3 E and S3 D**). Cells included in this subset also exhibited evidence of
245 cytotoxic function through the expression of *GZMA*, *GZMB* and *GNLY* transcripts, albeit
246 expression was also detected in CD8+ T-cells and activated tissue resident memory T cells (TRM)
247 (Clusters 1,3,4, **Fig. 3 E and S3 D**). Given the proximity of this cluster with myeloid lineages (**Fig.**
248 **2A and E**) and evidence of expression of macrophage-enriched transcripts, we referred to this
249 unique cluster as Macrophage-like T-cells (MTC). MTC also exhibited upregulation of key gene
250 pathways related to COVID-19, SARS-CoV-2 cell-intrinsic immune responses, cellular cytotoxicity
251 (e.g., degranulation) and cell death, consistently with a role for this subset to serve as a robust
252 primary responder to viral infection. (**Fig. 3 D**). Collectively, our findings suggest a potential role
253 for this previously uncharacterized subset in contributing to early control of SARS-CoV-2 infection
254 in lung tissues.
255
256 **Extravascular CD163+ inflammatory monocytes are the dominant antiviral mediator among**
257 **myeloid lineages**

258 Prior work has shown that the regulation of myeloid cells and their responses play a critical role
259 in the progression of SARS-CoV-2 related disease (Delorey et al., 2021a; Junqueira et al., 2022;
260 Rendeiro et al., 2021; Wauters et al., 2021); therefore, we investigated how myeloid lineages
261 respond to SARS-CoV-2 infection in fLX. Sub-clustering of myeloid lineages unveiled diverse
262 subpopulations, including alveolar and interstitial macrophages, various monocytes subsets, and
263 one conventional dendritic cell subset (cDC) (**Fig.4 A; Fig. S5**). Notably, we found the 2 dpi-
264 specific, viral RNA-enriched myeloid subset, earlier referred to as Cluster C, (see **Fig.2 B,E**) to
265 bear a signature of inflammatory monocytes (iMO) (**Fig.4 A-C**). iMO exhibited elevated
266 expression of *VCAN, S100A8, CD14, CD163* and absence/minimal expression of *CD4, MARCO*
267 *and CD206 (MRC1)* (**Fig. 4 D,E,F; Fig S4**). This gene expression profile was consistent with
268 those of human lung monocytes previously reported in human-immune system engrafted mice
269 (Evren et al., 2021) and human FCN1-monocytes recovered from the BAL of COVID-19 patients
270 with acute respiratory disease syndrome (Wendisch et al., 2021), collectively underscoring the
271 non-classical, extravascular monocyte nature of iMO and their human relevance in COVID-19.
272 Upon acute infection, only iMO and alveolar macrophages increased in frequencies, whereas
273 cDC and interstitial macrophage frequencies decreased (**Fig. 4 G**). iMO were the most abundant
274 lineage at 2 dpi (33.5%; **Fig. 4 G**) and were the leading mediators of antiviral responses, as
275 exemplified by the robust upregulated expression of interferon stimulated genes (ISGs) and
276 inflammatory cytokines (*CCL8, CXCL10, CCL2, ISG15, DEFB1, IL1RN, IFIT1, ISG20, IFIT3,* and
277 *MX1*), as well as inflammatory markers such as *CD163* (**Fig. 4 D,H**). While some ISGs (e.g.,
278 *ISG15, IFIT3, and MX1*) were expressed in other myeloid lineages at 2 dpi, their expression was
279 markedly lower compared to iMO, suggesting a strong association between viral RNA and
280 potentiated antiviral responses. Notably, upregulation of *CCL8*, *CXCL11* and *DEFB1* transcripts
281 were the most exclusive to iMO (**Fig. 4 H**). Decreased *CD4* expression was a defining feature of
282 iMO among monocyte sublineages (**Fig. 4 E**), suggesting that iMO differentiation is associate with
283 loss of CD4 expression concomitantly with extravasation.

284 In addition to iMO, a large population of CD4+ CD163- CD206(MRC1)- patrolling monocyte
285 was detected at all time points (Cluster 0; **Fig. 4 A,D,E**). This subset was however dominant at
286 12 dpi over other monocyte subsets (50.3%; **Fig. 4 G**), underscoring tissue repair and anti-
287 inflammatory mechanisms following viral clearance. Notably, a recent study provided evidence
288 for circulating patrolling monocyte to give rise to a non-classical, extravascular monocyte
289 population in the mouse lung that expand upon stimuli (Schyns et al., 2019), suggesting that
290 recruitment of CD4+ patrolling monocyte in BLT-L mice upon infection may be a pre-requisite for
291 extensive iMO differentiation and extravasation.

292 Multiplex immunohistochemistry (mIHC) analysis was consistent with our scRNAseq data.
293 While naïve fLX displayed high numbers of CD4+ cells and detectable CD163+ interstitial cells
294 (likely macrophages), acute infection at 2 dpi showed an increase in CD163+ cells both in the
295 extravascular interstitium and alveolar spaces and a dramatic reduction in CD4+ cells (**Fig. 4 I**).
296 These dynamics mirrored the 2 dpi-specific expansion of CD163+ iMO and alveolar macrophages
297 uncovered through scRNAseq. CD3+ T-cell lymphoid depletion was also apparent at 2 dpi (**Fig.**
298 **4 I**). At 12 dpi, the number of CD4+ cells had resolved reflecting the expansion of CD4+ patrolling
299 monocytes while the amount of CD163+ was reduced compared to 2 dpi (**Fig. 4 I**).

300 We also examined whether viral RNA-associated iMOs (CoV-iMOs) displayed specific
301 transcriptomic signature compared to iMOs (noCoV-iMOs) with undetectable viral RNA. Notably,
302 only two genes correlated with the presence of viral RNA in iMOs: *FGL2 and C15orf48* (**Fig. 4 J**).
303 While *FGL2* was down-regulated in CoV-iMO compared to noCoV-iMOs, *C15orf48* was
304 upregulated. Soluble FGL2 is known to exert immunosuppressive functions (notably through
305 inhibition of the NF-kB pathway) (Fu et al., 2023) whereas C15orf48 is a positive regulator of
306 inflammation previously associated with severe COVID-19 (Clayton et al., 2021). Collectively,
307 these findings suggest that productive or abortive SARS-CoV-2 infection could further potentiate
308 iMO inflammation through a specific set of genes.

309

310 **Systemic depletion of CD4+ cells abrogates viral clearance in fLX.**

311 To test the hypothesis that CD4+ monocyte recruitment is critical for SARS-CoV-2 clearance
312 in fLX, we performed systemic depletion of CD4+ cells through intraperitoneal injection of an anti-
313 CD4 antibody, both, prior to and after infection (**Fig. 5 A**). In parallel, we conducted depletion of
314 CD3+ or CD8+ cells in separate animal cohorts and in a similar manner to deconvolute the role
315 of T-cells and CD4+ non-T-cells in driving SARS-CoV-2 clearance. Effective systemic depletion
316 was confirmed in the blood by flow cytometry (**Fig. S5 A**), and all animals were euthanized at 12
317 dpi to probe for persistent SARS-CoV-2 infection in fLX. fLX isolated from CD4-depleted animals
318 exhibited robust persistence of productive SARS-CoV-2 infection at 12 dpi (mean Log PFU/mg
319 tissue=2.37), and to a more significant extent than CD3- and CD8-depleted animals (mean Log
320 PFU/mg tissue=0.96 and 0.83, respectively) when compared to IgG isotype treated mice (mean
321 Log PFU/mg tissue=0) (**Fig. 5 B**). Notably, persistent infection in CD4-depleted animals was
322 associated with significant downregulation of MHC class I (**Fig. 5 C**), a phenomenon we similarly
323 observed in acutely infected fLX (2 dpi) (**Fig. 5 C**) and within our scRNAseq dataset (**Fig. 2 H**)
324 and that has been previously reported in cells actively replicating SARS-CoV-2 (Arshad et al.,
325 2023; Yoo et al., 2021), further emphasizing that depletion of CD4+ cells is associated with
326 persistent viral replication.

327 Using mIHC, we validated the absence of CD4+ cells in fLX at 12 dpi. CD163+ cells were also
328 consistently reduced in the fLX of CD4-depleted animals compared to the fLX of animals treated
329 with IgG isotype control antibodies (**Fig. 5 D**[a,d,e]). In CD4-depleted mice, the remaining CD163+
330 cells co-localized with PPARγ+ cells, indicating that lung alveolar macrophages are not effectively
331 depleted by systemically-delivered antibodies (**Fig. 5 D**[d-e]). Furthermore, some fLX from CD4-
332 depleted mice appeared more enriched in CD3+ CD4- cells compared to isotype-treated mice
333 (**Fig. 5 D**[e]), suggesting that defective monocyte recruitment may lead to enhanced CD8+ T-cell
334 recruitment. CD3- and CD8-depleted mice that successfully cleared infection exhibited a higher
335 presence of CD163+ cells in fLX at 12 dpi compared to isotype-treated mice, indicating that the

336 absence of CD8+ T-cells may lead to increased monocyte recruitment for effective viral clearance
337 (**Fig. 5 D**[b-c,f-g]).
338 Collectively, our findings suggest that the recruitment of CD4+ monocyte into infected fLX is
339 a crucial mechanism associated with effective viral clearance.
340
341 **Depletion of CD4+ cells in BLT-L mice recapitulates features of chronic viral infection**
342 We then investigated whether persistent SARS-CoV-2 infection at 12 dpi in CD4-depleted mice
343 displayed similarities with acute infection (i.e., at 2 dpi), or bore hallmarks of chronic viral infection.
344 Both acutely infected mice (2 dpi) and CD4-depleted mice (12 dpi) displayed similarly elevated
345 serum levels of CCL2 and CCL3 (**Fig. 5 E,F**) which contrasted with protein levels found in naïve
346 mice and those that resolved infection. Given the importance of CCL2 and CCL3 as monocyte
347 chemoattractants, these findings further support the hypothesis that acute SARS-CoV-2
348 replication in fLX is associated with effective recruitment of circulating monocytes. To identify the
349 potential source of CCL2 and CCL3 expression in fLX upon acute infection, we returned to our
350 scRNAseq data. While *CCL2* and *CCL3* transcripts were detectable in several fLX human
351 lineages at naïve state (mesenchymal and endothelial for *CCL2*, and T-cell and myeloid for *CCL3*)
352 (**Fig. S5 B,C**), three major sources of CCL2 transcripts emerged at 2 dpi, namely iMO, MTC and
353 interstitial macrophages (**Fig. S5 B)**. No significant transcriptomic upregulation of *CCL3* was
354 detected in fLX consistently with previously reported mechanisms of post-transcription regulation
355 (Kang et al., 2011; Mao et al., 2019). Unlike CCL2 and CCL3, serum levels of CXCL10 were only
356 elevated in acutely infected mice (2 dpi) but not in CD4-depleted mice at 12 dpi (**Fig. 5 G**). This
357 finding is consistent with evidence that iMO are major source of CXCL10 (**Fig. 4 E**), and that iMO-
358 mediated inflammation is associated with effective viral clearance.
359 Notably, persistently infected mice can be distinguished from acutely infected (2 dpi) and
360 isotype-treated (12 dpi) mice by elevated levels of CCL19 in serum (**Fig. 5 H**). CCL19 is a pro-
361 inflammatory cytokine that has been linked with persistent viral replication and inflammation such

362 as in the context of HIV-1 infection (Damas et al., 2009), underlining that persistent SARS-CoV-
363 2 infection in BLTL-L mice recapitulate key immunological features of chronic viral infection.
364 Unlike acutely infected fLX, persistently infected fLX did not display any significant
365 histopathological manifestations of disease (**Fig. 5 I**). While the lack of CD4+ cells and reduced
366 inflammation could promote such an outcome, we have previously reported that fLX exhibit
367 significant histopathological manifestations of disease upon SARS-CoV-2 infection even in the
368 absence of engraftment of a human immune system (Kenney et al., 2022). These findings suggest
369 that persistent SARS-CoV-2 infection remodels the lung tissue environment to better tolerate
370 sustained viral replication.
371 Lastly, it has been suggested that persistent SARS-CoV-2 infection can give rise to stable
372 mutations and eventually, to novel variants (Machkovech et al., 2024; Maponga et al., 2023).
373 While we failed to acquire viral reads of acceptable quality from persistently infected fLX at 12
374 dpi, we successfully recovered viral genome sequences from acutely infected fLX at 2 dpi, prior
375 to infection resolution. 75% of 2 dpi-associated viral sequences exhibited the selection of two
376 stable mutations not observed in our inoculum and located in the Spike N-terminal domain (NTD):
377 an insertion (216KLRS) and a non-synonymous mutation (R245H) (**Fig. 5J,K**; **Table S1**.
378 Interestingly, these two mutations were found together in 100% of the viral sequences, suggesting
379 potential co-evolution (**Fig. 5L**), and have been reported as positively selected in the context of
380 sub-optimal neutralizing antibody concentration (216KLRS) (PMDA, 2021) or in the context of
381 cross-species adaptation (216KLRS and R245H) (Fagre et al., 2021). The ability of SARS-CoV-
382 2 proteins to undergo rapid mutational selection with reported functional relevance strongly
383 support the potential of BLT-L mice to predict viral adaptation associated with persistent infection
384 and the potential emergence of novel variants.
385
386 **Non-hematopoietic responses to infection likely contribute to effective resolution.**

387 Finally, we aimed to further leverage our scRNAseq datasets to examine the contribution of
388 the mesenchymal and endothelial compartment in mediating effective infection resolution.
389 Relative expansion of the mesenchymal compartment upon infection was mainly driven by an
390 increase in fibroblast populations (**Fig. 2 C; Fig. 6 A-C**). An increase in alveolar fibroblasts was
391 observed at 12 dpi (49.6%; naïve=28.1%) which was preceded by the emergence of a 2 dpi-
392 specific cluster of activated fibroblasts (26.5%; naïve=8.9%), consistent with effective tissue repair
393 in response to lung damage (**Fig. 6 A-C**). Activated fibroblasts were the dominant mesenchymal
394 population during antiviral responses, as displayed by robust upregulation of interferon stimulated
395 genes (*LY6E*, *BST2*, *ISG15* and *IFI44L*; (**Fig. 6 D**) and cytokine signatures, which included major
396 pro-inflammatory mediators such as *CXCL10* and *TIMP1* (**Fig. 6 E-G**). Elevated expression of
397 mitochondrial encoded genes at 12 dpi was also observed, which we hypothesize to be reflective
398 of high metabolic activity.

399 The endothelial compartment is an important modulator of immune recruitment through
400 cytokine/chemokine signaling. Infected fLX showed the emergence of an activated, 2 dpi-specific
401 endothelial cell cluster (**Fig. 6 H,I**), which was identified by increased expression of several
402 transcripts involved in myeloid chemotaxis (**Fig. 6 J, Fig. S5 D**), including *CXCR4* and *MCAM*
403 (Gupta et al., 1998; Leroyer et al., 2019). In addition, transcripts of INSR, which can
404 downregulates CXCR4 expression through binding with insulin (Payankaulam et al., 2019;
405 Rathjen et al., 2022), were also found to be upregulated (**Fig. 6 J, Fig. S5 E,F**).

406 Venous endothelial cells displayed significant upregulation of a panel of interferon-stimulated
407 gene transcripts (*XAF1, IFIT1, MX1, IFI44L, RSAD2)* at 2 dpi (**Fig. 6 L**) underscoring an active
408 antiviral response. Downregulation of several transcripts coding for activation markers (*CD69*),
409 MHC genes (*HLA-DPB1, HLA-C*) and major proteins regulating cellular metabolism and
410 transcription (*HSP90AA1, RPL13A*) was reflective of endothelial dysfunction and stress (**Fig. 6**
411 **L**); consistent with human patient reports and animal studies (Kadiyska et al., 2022; Otifi and
412 Adiga, 2022; Qin et al., 2021; Xu et al., 2023). At 12 dpi, venous endothelial cells upregulated

413 expression of mitochondrial genes, which was similar to the transcriptomic pattern of activated
414 fibroblasts. Increases in mitochondrial transcripts were also observed in other endothelial clusters
415 (lymphatic endothelial cells and capillary cells) at 12 dpi (**Fig. 6 L**). This consistent finding across
416 multiple cell types in the endothelial compartment highlights the elevated metabolic activity
417 associated with tissue repair following infection resolution.

418 Collectively, BTL-L mice recapitulate a wide panel of cellular and transcriptomic hallmarks of
419 SARS-CoV-2 pulmonary infection observed in COVID-19 patients, and support a contribution of
420 the endothelium in driving infection resolution by enhancing monocyte recruitment.

421

422 **DISCUSSION**

423 As our appreciation of the immunological differences between mice and humans continue to grow,
424 humanized mouse models are increasingly standing out as robust platforms to understand how
425 viral pathogens interact with human tissues, and with the human immune system. These models
426 are especially valuable when investigating tissue and mucosal immunity, since such
427 investigations remain impractical in human patients.

428 The SARS-CoV-2 pandemic has emphasized the need to increase our understanding of an
429 effective, or failing, pulmonary immune responses during coronavirus infection. Mice engrafted
430 with human immune systems and genetically matched human lung tissues are valuable
431 alternatives to investigate lung-resident human immune responses to coronavirus infection (Di et
432 al., 2022; Kenney et al., 2022; Sun et al., 2022a; Wahl et al., 2019), bridging the limitations of
433 conventional animal models and the challenges associated with human studies. Using the HNFL
434 mouse model, we previously reported that such models can be leveraged to capture
435 immunological signatures defining effective control of SARS-CoV-2 infection (Kenney et al.,
436 2022). However, the enhanced myeloid reconstitution of the HNFL model rapidly inhibits
437 extensive viral replication in fLX, precluding our ability to study protective immunological
438 mechanisms that are at play upon acute, and potentially symptomatic, infection.

439 The goal of this study was to fill in this knowledge gap and uncover the array of lung-resident
440 immune mechanisms promoting effective control of acute SARS-CoV-2 infection. In contrast to
441 the HNFL mouse model, we postulated that the lesser myeloid engraftment and the more
442 prominent lymphoid reconstitution of BLT-L mice would enable us to more effectively mimic acute
443 infection and subsequent resolution in a human immunocompetent context. Consistently, BTL-L
444 mice were effectively able to clear both infectious viral particles and viral RNA following an early
445 peak of viral replication in fLX. Infection resolution was associated with a rapid mobilization of the
446 human immune cells into fLX upon viral inoculation, which aligns with previous evidence that
447 immunodeficient mice only engrafted with fLX are unable to clear infection (Kenney et al., 2022;
448 Wahl et al., 2021).
449
450 Here we identified two major hallmarks of protective lung-resident human immune responses
451 to SARS-CoV-2 infection. The first was the transient differentiation of circulating monocytes as
452 extravascular iMO and their role as primary mediators of antiviral responses. To the best of our
453 knowledge, this study represents the initial evidence of a direct role played by human lung
454 extravascular inflammatory monocytes in the resolution of respiratory viral infections. Several
455 lines of evidence support the monocyte nature of these cells. This include their close
456 transcriptomic proximity with patrolling monocytes which have been reported to give rise to
457 transient, extravascular (including alveolar) monocytes in the mouse lung (Schyns et al., 2019),
458 as well as their resemblance to monocytes reported in the BAL of COVID-19 patients (Wendisch
459 et al., 2021) and from the lung of human-immune system engrafted mice at steady state (Evren
460 et al., 2021).
461 The upregulation of myeloid recruitment signals and chemokines, including CCL2 and CCL3,
462 suggested a strong association between infiltration of circulating monocytes and iMO
463 differentiation. Abrogation of effective viral clearance following systemic depletion of CD4+
464 monocytes, but not CD3+ T-cells, was consistent with this model. Elevated serum levels of CCL2

465 and CCL3 persisted at 12 dpi in CD4-depleted animals, unlike mice that cleared infection at a
466 similar time point, further underscoring a connection between active viral replication and
467 monocyte recruitment signals in fLX. While iMO were identified as a substantial source of *CCL2*
468 transcripts at 2 dpi, CCL2 serum concentration was similarly elevated between CD4-depleted
469 animals (12 dpi) and non-depleted acutely infected animals (2 dpi) suggesting that MTC may
470 compensate for limited CCL2 production in absence of defective iMO differentiation during
471 infection.

472 The second hallmark of effective control of SARS-CoV-2 infection in fLX that we identified was
473 the detection of MTC, a T-cell population highly enriched in viral RNA. MTC exhibited expression
474 of key macrophage-defining genes and elevated cytotoxic activity. While this population presents
475 some similarity with innate-like T-cells (Molgora and Colonna, 2022), which harbor cytotoxic
476 signatures and whose roles in cancer have been investigated, MTC appear to be unique given
477 their combination of lymphoid, myeloid and mesenchymal markers and their short-lived, apoptotic
478 nature suggested by their complete absence at 12 dpi. MTC also share transcriptomic similarities
479 with γδ T-cell subsets previously described as bearing myeloid and cytotoxic functions (Lebedev
480 et al., 2021; Muto et al., 2015). However, their expression of conventional macrophage makers
481 emphasizes their uniqueness. Additional investigation is required to better our understanding of
482 the identity and functions of this potentially novel cell subset. However, it is tempting to speculate
483 that MTC may uniquely synergize CD8+ cytotoxic T-cell functions with viral particle phagocytosis
484 to effectively control infection prior to undergoing rapid cell death.

485

486 Severe COVID-19 has been associated with elevated macrophage infiltration, inflammatory
487 responses and profibrotic phenotypes (Delorey et al., 2021a; Rendeiro et al., 2021; Wauters et
488 al., 2021; Wendisch et al., 2021), supporting an overall picture in which excessive myeloid
489 inflammation and fibrotic response -despite promoting infection resolution- drive potentially fatal
490 acute respiratory distress syndrome (ARDS) and fibrosis. SARS-CoV-2 can trigger abortive

491 infection of both monocytes and macrophages (Boumaza et al., 2021b; Junqueira et al., 2022;
492 Yang et al., 2020; Zheng et al., 2021), and viral RNA replication and protein production in these
493 cells results in inflammasome activation and exacerbated inflammation (Junqueira et al., 2022;
494 Munnur et al., 2021; Sefik et al., 2022). However, we observed that viral RNA in iMO was
495 associated with tissue protection, transient and balanced inflammation (with no inflammasome
496 activation). By 12 dpi and infection resolution, fLX were nearly devoid of iMO but enriched in
497 patrolling monocytes. In mice, patrolling monocytes can give rise to lung extravascular
498 monocytes, which exhibit a dynamic transition state and can differentiate into CD206- interstitial
499 macrophages (Schyns et al., 2019). Our findings, in conjunction with reports indicating that severe
500 COVID-19 correlates with the persistence of monocyte-derived profibrotic macrophages
501 (Wendisch et al., 2021), suggest that the rapid reversion of iMO toward a patrolling phenotype
502 following encounter with viral RNA, rather than differentiation into interstitial macrophages,
503 represents a hallmark of protection from COVID19 disease. The limited antiviral responses and
504 major population contraction of interstitial macrophages at 2 dpi (**Fig. 4 B, D**) supported the notion
505 that circulating monocytes and/or iMO are not extensively differentiating into interstitial
506 macrophages upon infection.
507
508 The contribution of T-cells in infection resolution in our model remains elusive, particularly in light
509 of the inability of CD3-depleted mice to fully clear infection (50% of animals cleared infection). It
510 is worth noting that even when viral infection persisted in CD3-depleted animals, viral titers in fLX
511 remained significantly lower than in the fLX of persistently infected CD4-depleted animals (**Fig.
512 S5 G**). This suggests that CD4+ cells, mainly monocytes rather than T-cells, are critical to viral
513 clearance. Our mIHC data supports this hypothesis by revealing greater numbers of CD163+ cells
514 in fLX of CD3-depleted mice that were able to effectively clear infection at 12 dpi compared to
515 those that remained persistently infected. Therefore, while T-cells may contribute to viral
516 clearance, their absence could be compensated by increased iMO responses of various

517 magnitudes, ultimately resulting in complete or partial viral clearance. Given the significant
518 lymphoid depletion observed in fLX at 2 dpi and the limited antiviral responses mounted by CD4+
519 and CD8+ T-cells, one could then postulate that CD3+ T-cell depletion may interfere with the
520 differentiation and/or effective function of MTC in infected fLX, and that the lack of MTC may be
521 totally or partially compensated by a more extensive iMO response. How CD3+ depletion may
522 impact MTC, and how MTC and iMO functions may synergize to effectively control infection and
523 prevent extensive inflammation-induced tissue damage will need to be investigated.
524
525 Our data suggest a unique immunological model that defines cellular mechanisms leading to
526 effective control of SARS-CoV-2 infection in the human lung (**Fig. 7**). Upon SARS-CoV-2 infection
527 of fLX, initial epithelial infection triggers the activation of fibroblasts and endothelial cells. While
528 fibroblasts potentiate initial myeloid inflammatory responses, endothelial activation and CCL2
529 secretion by MTC drives the recruitment of patrolling monocytes, which subsequently differentiate
530 into iMO. iMO then exert a bimodal function: they "sponge" viral particles and components, and
531 exert tissue-wide antiviral responses protecting the epithelial compartment from *de novo* infection.
532 In parallel, MTC independently complement the "sponging" functions of iMO by adsorbing viral
533 particles. A defining hallmark of mild disease is the ability of patrolling monocyte to transiently
534 differentiate into iMO prior to reverting back into a patrolling monocyte state, instead of upholding
535 an inflammatory phenotype and further differentiating into inflammatory interstitial macrophages.
536 Several aspects of this model will need to be further investigated. Understanding the cellular
537 and molecular drivers defining the fate of infiltrating monocytes upon exposure to SARS-CoV-2,
538 and how key regulatory cross-roads in this cell type define the course of disease, is of particular
539 interest. Compounding immune dysregulations, such as elevated inflammatory baseline and/or
540 specific myeloid imprinting, may contribute to monocyte's inability to adequately regulate their
541 activation in a timely manner upon encountering viral materials, leading to rapid differentiation
542 into macrophages and exacerbated inflammation. Investigating the role of fibroblast and

543 endothelial activation in driving effective clearance mechanisms as well as these cells'
544 contribution to iMO differentiation is also of particular significance. It remains unclear as to how
545 endothelial and fibroblasts are activated during infection as neither cell population displayed signs
546 of viral RNA enrichment. Whether activation of these cells is triggered indirectly by early epithelial
547 and/or myeloid activation, or via direct exposure to viral components such as the nucleocapsid
548 protein (Qian et al., 2021) could be investigated using the BLT-L mouse model.
549
550 Patients suffering from immunodeficiencies can experience persistent SARS-CoV-2 replication in
551 the respiratory tract for over 100 days (Abe et al., 2021; Hettle et al., 2022; Sepulcri et al., 2021).
552 Persistent infection in immunodeficient individuals has a strong public heath significance, since
553 extended periods of replication in a single host has been postulated to favor the emergence of
554 variants of concern (Hettle et al., 2022; Shrestha et al., 2022). The ability of the BLT-L mouse
555 model to recapitulate productive and persistent SARS-CoV-2 infection in human lung tissues
556 through induction of a specific immunodeficiency opens avenues to dissect viral and host
557 adaptations favoring viral persistence in a human tissue context. Further, this could shed light into
558 how these adaptations can contribute to viral evolution and antigenic divergence. Persistent
559 SARS-CoV-2 infection in BLT-L mice associated with three major features: (1) persistent CCL2
560 and CCL3 production, (2) absence of lung histopathological manifestation of disease and (3)
561 elevated serum concentration of CCL19.
562 CCL19 can potentiate antiviral immune responses by promoting dendritic cell and T-cell
563 migration into lymph nodes through CCR7 binding (Yan et al., 2019). However, the CCR7-CCL19
564 axis can also contribute to viral pathogenesis as elevated serum levels of CCL19 correlate with
565 severe COVID-19 (Tveita et al., 2022) and persistent inflammation in untreated HIV-1 patients
566 (Damas et al., 2009). For instance, CCL19 mediated inflammation can enhance immune tolerance
567 by promoting CCR7 internalization (Kohout et al., 2004) and anti-inflammatory signaling (Serrano-
568 Lopez et al., 2021).

569 Our current knowledge on CCL19 functionality during viral infection suggests that persistent
570 infection in BLT-L mice drives tissue remodeling processes typical of chronic inflammation and
571 potentiates mechanisms of immune tolerance. Histopathological manifestations of disease in fLX
572 upon acute SARS-CoV-2 infection are persistent in mice engrafted solely with fLX (Kenney et al.,
573 2022; Wahl et al., 2020) but are transient in BTL-L mice, underscoring that such cytopathic
574 manifestations are not driven by human hematopoietic cells but rather by extensive viral
575 replication. Thereby, the absence of histopathological manifestations of disease observed in fLX
576 upon persistent SARS-CoV-2 replication (**Fig. 6 I**) support evidence of a tissue-wide remodeling
577 toward viral tolerance. The remarkable ability of BLT-L mice to support the rapid emergence of
578 adaptive mutations in the viral genome previously reported to confer increased fitness *in vitro* and
579 *in vivo*, emphasizes the strong potential of this mouse model to recapitulate not only host, but
580 also viral adaptations underlying persistent SARS-CoV-2 infection and to predict potential
581 evolutionary courses.
582
583 It is important to note that there are inherent limitations associated with the BLT-L mouse model.
584 First, direct viral inoculation into fLX potentially bypasses key immune checkpoints in the upper
585 respiratory tract, which are not recapitulated in our model. Second, the hematopoietic
586 reconstitution and functions of the BLT-L mouse model remain imperfect, notably through the
587 underrepresentation of specific hematopoietic subsets, including dendritic cells and granulocytes,
588 and limited B-cell responses – which may ultimately bias the dynamics of viral clearance. Despite
589 these limitations, BLT-L mice recapitulated human lung responses to SARS-CoV-2 infection
590 through AT2 loss of programming, fibroblast and endothelial activation, effective clearance of
591 infection through robust hematopoietic responses. This mouse model also supported viral
592 adaptation processes with public health relevance, and recapitulated signatures of persistent viral
593 replication that are consistent with patients suffering from chronic infection. Together, our work
594 unravels the potential of the BLT-L mouse model to uncover critical human mechanisms

595 governing effective resolution of coronavirus infection. It highlights the value of this mouse model
596 to identify novel immunotherapeutic strategies against coronaviral diseases and enhance our
597 comprehension of the host and viral mechanisms underlying SARS-CoV-2 persistent infection
598 and evolution.
599

600 **MATERIALS AND METHODS**

601 ***Institutional approvals***

602 All animal experiments described in this study were performed in accordance with protocols that
603 were reviewed and approved by the Institutional Animal Care and Use and Committee of the
604 Ragon Institution and Boston University (PROTO202000020). All mice were maintained in
605 facilities accredited by the Association for the Assessment and Accreditation of Laboratory Animal
606 Care (AAALAC). All replication-competent SARS-CoV-2 experiments were performed in a
607 biosafety level 3 laboratory (BSL-3) at the Boston University National Emerging Infectious
608 Diseases Laboratories (NEIDL).
609

610 ***Resources***

611 ***Mouse strains.*** Female NOD.Cg.-*Prkdc*^{Scid}*Il2rg*^{tm1Wjl}/SzJ (NSG) mice were obtained from the
612 Jackson Laboratory, catalog number 005557. NSG mice were maintained by the Ragon Institute
613 Human Immune System Mouse core prior to engraftment and shipment to the NEIDL, Boston
614 University.
615

616 ***Human fetal tissues.*** De-identified human fetal tissues were procured from Advanced Bioscience
617 Resources (Alameda, CA, USA).
618

619 ***Cell lines.*** VeroE6 cells were grown in Dulbecco's modified Eagle's medium (DMEM)
620 supplemented with 10% heat inactivated fetal bovine serum (Bio-Techne, R&D systems,

621 Minneapolis, MN, USA) and 1% (v/v) Penicillin Streptomycin (Thermo Scientific, Waltham, MA,
622 USA).
623
624 ***Antibodies.*** The anti-mouse antibody CD45-PE-Dazzle5 clone 30-F11 was purchased from
625 BioLegend (San Diego, CA, USA) and used for flow cytometry. The following anti-human
626 antibodies were used for flow cytometry and were all acquired from BD Biosciences (San Jose,
627 CA, USA): HLA-DR-BV510 clone L243, CD3-BV605 clone UCHT1, CD20-BV650 clone 2H7,
628 CD16 (FcγRIII)-BV117 clone B73.1, CD45-BV785 clone H130, CD8-FITC clone RPA-T8, CD33-
629 PE clone WM53, CD14-PerCP-Cy5.5 clone HCD14, CD45RA-PE-Cy7 clone HI100, CD56-
630 allophycocyanin clone QA17A16, CD4-Alexa Fluor 700 clone SK3. The following anti-human
631 antibodies were used for *in vivo* depletions: From Bio-X Cell (Lebanon, NH, USA): anti-human
632 CD3 clone OKT3, anti-human CD4 clone OKT4, anti-human CD8 clone OKT8; From
633 Thermofisher: mouse IgG2a isotype. The anti-SARS-CoV-2 (2019-nCoV) Spike RBD-mFc clone
634 #57 used as a control for neutralization assays was acquired from Sino Biologicals.
635
636 ***Experimental methods***
637 ***Generation of BLT-L mice.*** BLT mice were generated via irradiation of female NOD.Cg.-
638 *Prkdc*^{Scid}*Il2rg*^{tm1Wjl}/SzJ mice (NSG mice; Jackson Laboratory #005557) with 200 rads from an X-
639 ray irradiator. Mice then underwent surgery to implant 1mm^3 of human fetal thymic and fetal liver
640 tissue (Advanced Bioscience Resources) under the murine kidney capsula. After the blunt
641 resection of the thoracal subcutis, through the same surgical opening, two pieces of homologous
642 human fetal lung tissue into the subcutaneous dorsal area of the 8-15 week old females. Post-
643 implantation, mice intravenously received 1x10^5 homologous CD34+ cells. Human immune
644 reconstitution was determined by flow cytometry at weeks post implantation. Three distinct human
645 donors were used for this study.
646

647 ***Generation of SARS-CoV-2 isolate and recombinant SARS-CoV-2 NanoLuc viral stocks.*** All
648 replication-competent SARS-CoV-2 experiments were performed in a BSL-3 facility at the Boston
649 University National Emerging Infectious Diseases Laboratories. The clinical isolate named 2019-
650 nCoV/USA-WA1/2020 strain (NCBI accession number: MN985325) of SARS-CoV-2 was
651 obtained from BEI Resources (Manassas, VA, USA). Recombinant SARS-CoV-2 expressing
652 NanoLuc Luciferase (rSARS-CoV-2 NL) (Xie et al., 2020) was graciously provided by the
653 Laboratory of Pei-Yong Shei. Viral stocks were grown and purified as previously described
654 (reference HNFL manuscript). Briefly, $1x10^7$ Vero E6 cells were plated in a T-175 flask the day
655 prior to virus generation. The next day, cells were infected with virus diluted in 10 mL of Opti-MEM
656 (ThermoFisher Scientific, Waltham, MA, USA) and incubated for 1 h at 37°C to allow for virus
657 adsorption. After 1 h, 15 mL of DMEM containing 10% FBS and 1% penicillin/streptomycin was
658 added to cells and incubated overnight. The next day, media was removed, cells were rinsed with
659 1X PBS, pH 7.5 (ThermoFisher Scientific) and 25 mL of fresh DMEM containing 2% FBS was
660 added. Cells were assessed for cytopathic effect (CPE), media was collected, filtered with a 0.22
661 µm filter, and concentrated by sucrose gradient. Concentrated virus was suspended in sterile 1X
662 PBS, pH 7.5, aliquoted and stored at –80C.
663
664 ***Viral quantification by plaque assay.*** The titer of our viral stocks was determined by plaque
665 assay. Vero E6 cells were seeded into a 12-well plate at a density of $2x10^5$ cells per well. The
666 next day, cells were infected with 10-fold serial dilutions of the viral stocks and incubated for 1
667 hour at 37°C to allow for viral adsorption. After 1 hour incubation, 1 mL of overlay media (1.2%
668 Avicel (DuPont, Wilmington, DE, USA; RC-581) in DMEM supplemented with 2% FBS and 1%
669 Pen/Strep) was added to each well. Three days later, the overlay media was removed, and cells
670 were fixed for 1 hour at room temperature with 10% neutral buffered formalin (ThermoFisher
671 Scientific). Formalin was removed after fixation and cells were stained for 30 min at room
672 temperature with 0.1% crystal violet (Sigma-Aldrich) prepared in 10% ethanol/water. Crystal violet

673 was removed, cells were washed with water and plaque forming unites were counted to determine
674 viral titers.
675
676 ***Mouse inoculation with SARS-CoV-2.*** BLT-L mice were anesthetized with 1–3% isoflurane prior
677 to inoculation via subcutaneous, intra-fetal lung xenograft (intra-fLX) injection with 10^6 plaque
678 forming unites (PFU) of SARS-CoV-2 WA-1 isolate in 50 µL of sterile 1X PBS. Mice were
679 euthanized at 2-, 6-, and 12-days post inoculation.
680
681 ***In vivo antibody depletion.*** BLT-L mice were administered 200 mg of anti-CD3e (OKT3)
682 (BioxCell; cat. # BE0001-2), anti-CD4 (OKT4) (BioxCell; cat. # BE0003-2), anti-CD8 (OKT8)
683 (BioxCell; cat. # BE0004-2), or isotype IgG2a (Thermofisher; cat # 02-6200) antibody 3-, 2-, and
684 1-day prior to inoculation and 4- and 8-days post inoculation with $1x10^6$ PFU SARS-CoV-2 WA-
685 1.
686
687 ***Generation of single cell suspension from mouse blood.*** Blood processing was performed as
688 previously described (Kenney et al (2022) *Cell Reports*). Briefly, blood was collected via
689 submandibular bleeding or heart puncture and transferred into EDTA capillary collection tubes
690 (Microvette 600 K3E; Sarstedt, Nümbrecht, Germany). Blood was centrifuged at 3,500 RPM for
691 10 minutes at room temperature, serum was removed, and whole blood was subject to ACK lysing
692 (ThermoFisher Scientific; #A1049201) for 10 minutes at room temperature. Lysing was quenched
693 with 10% (v/v) FBS DMEM media and cells were washed twice with a 1% (v/v) FBS-PBS solution
694 (FACS Buffer) before downstream processing.
695
696 ***Generation of single cell suspension from fLX.*** Fetal lung xenografts were processed as
697 previously described (Kenney et al., 2022). Briefly, lung tissues were placed in a 60 mm dish,
698 minced using a disposable scalpel, then transferred into a 15 mL conical tube containing 3 mL of

699 digestion buffer (HBSS minus Ca2+, Mg2+, and phenol red, 0.5 mg/mL Liberase TM, 1 mg/mL
700 DNase I) and incubated at 37°C for 30 min with agitation every 10 min. After digestion, tissue was
701 passed through a 70 µm strainer on a 50 mL tube, mashed using the plunger of a 3 mL syringe
702 and washed twice with 1 mL FACS buffer. Cell suspension was centrifuged at 300 *x g* for 5
703 minutes at 4°C, suspended in 1 mL of ACK lysing buffer, and incubated for 2 min at room
704 temperature. After incubation, lysis was quenched with 12 mL of FACS buffer, cell suspension
705 was centrifuged at 300 *x g* for 5 min at 4°C, and the cell pellet was suspended in 1 mL of FACS
706 buffer prior to downstream processing.
707
708 ***Viral RNA extraction from serum.*** Viral RNA was extracted from serum using a Zymo Viral RNA
709 extraction kit (Zymo Research, Irvine, CA, USA: #R1035) following the manufacturers protocol.
710 Briefly, serum was mixed with RNA/DNA shield (Zymo) at a 1:1 ratio. RNA buffer was then added
711 to the serum (2:1 ratio) and passed through a column by centrifugation at 13,000 x g. The column
712 was then washed twice, and RNA was eluted with 15 µL of RNase/DNase free water.
713
714 ***RNA extraction from fLX.*** During necropsy a piece of fLX tissue was placed in 600 µL of
715 RNAlater (MilliporeSigma: #R0901500ML) and stored at −80°C until analysis. For RNA extraction,
716 20–30 mg of tissue was weighed out, placed into a 2 mL tube with 600 µL of RLT buffer with 1%
717 β–mercaptoethanol and a 5 mm stainless steel bead (Qiagen, Hilden, Germany: #69989), then
718 dissociated using a Qiagen TissueLyser II (Qiagen) with the following cycle: two min dissociation
719 at 1800 oscillations/min, one min rest, two min dissociation at 1800 oscillations/min. Dissociated
720 tissues were centrifuged at 13,000 rpm for 10 min at room temperature and cleared supernatant
721 was transferred to a new 1.5 mL eppendorf tube. RNA extractions were performed using a Qiagen
722 RNeasy Plus Mini Kit (Qiagen: #74134), according to the manufacturer's instructions (Qiagen:
723 #79256). RNA was eluted in 30 µL of RNase/DNase free water and quantified by Nanodrop.
724

725 ***fLX processing for viral titer quantification.*** Tissue pieces stored in RNALater were thawed at
726 room temperature and then 22-40 mg of tissue were weighed out and placed into 600 uL of
727 OptiMEM (ThermoFisher Scientific). Tissues were homogenized using a Qiagen TissueLyser II
728 with two dissociation cycles, centrifuged and supernatant was transferred to a new 1.5 mL
729 Eppendorf tube (see "*RNA extraction from fLX" section*). Tissue homogenates were then serial
730 diluted (10^{-1} – 10^{-6}) and 300 uL of supernatant was plated on VeroE6 cells in 12-well plates ($2x10^5$
731 cells/well). Supernatant was incubated for 1 hour at 37°C to allow for viral adsorption then 1 mL
732 of a 1:1 mixture of 2X DMEM 4% FBS 2% penicillin/streptomycin and 2.4% Avicel (Dupont) was
733 overlaid onto each well. Plates were incubated for 72 hours at 37°C with 5% CO_2. Avicel was then
734 removed, cells were fixed in 10% buffered formalin (ThermoFisher Scientific) for 1 hour, then
735 stained with 0.1% crystal violet in 10% ethanol/H_2O for 30 minutes before washing and
736 quantification.
737
738 ***Serum neutralization assay.*** One day prior to the experiment, 1 × 104 Vero E6 cells were plated
739 into a 96-well plate. Serum was decomplemented at 56 °C for 30 min and an initial dilution of 1:10
740 was prepared in OptiMEM. Two-fold dilutions were subsequently prepared and mixed with
741 rSARS-CoV-2 NL virus (MOI = 1) for 1 h at room temperature and then plated onto cells. After a
742 1-h incubation at 37 °C inoculum was removed and 200 µL of fresh DMEM containing 2% FBS
743 and 1% penicillin/streptomycin was added. After a 24 h incubation at 37 °C with 5% CO2 media
744 was removed and cells were fixed with 10% formalin for 1 h. A SARS-CoV-2 spike neutralizing
745 antibody (Sino Biological Inc., Beijing, China; 2 µg/µL; Clone #57) was used as a positive control.
746 Cells were washed with 1× PBS and 20 µM furimazine (MedChem Express, Monmouth Junction,
747 NJ, USA) luciferin substrate was added onto cells. Cells were then imaged using an IVIS spectrum
748 imager (PerkinElmer) and analyzed using LivingImage software (PerkinElmer). Titers were
749 determined as the reciprocal of the highest dilution with >50% reduction of cytopathic effect.
750

751 ***Quantification of peripheral human chimerism in BLT-L mice.*** 2–4x10^6 PBMCs of human or
752 murine origin were isolated as described above and stained for 1 hour at 4°C in the dark with an
753 antibody cocktail targeting human(h)CD45, mouse CD45, hCD3, hCD4, hCD8, hCD16, hCD19,
754 hCD11c, hCD56 and hCD14. Following washing with FACS Buffer, cells were fixed with fixation
755 buffer (1% (v/v) FBS, 4% (w/v) PFA in PBS) for 30 min at 4°C in the dark. Chimerism of all
756 humanized mice was assessed by quantifying the following human populations: Human CD45+,
757 human CD45+ murine CD45-; T-cells, CD45+ CD3+; CD4+ T cells, CD45+ CD3+ CD4+; CD8+ T
758 cells, CD45+ CD3+ CD8+; CD45+ CD16+ leukocytes; B-cells, CD45+ CD19+; conventional
759 dendritic cells, CD45+ CD11c+; NK/NKT cells, CD45+ CD56+; Monocytes, CD45+ CD14+.
760
761 ***Antibody staining.*** After generation of single cell suspension, 5x10^5 - 1x10^6 cells were used for
762 flow cytometry staining. Cells were centrifuged at 300 X *g* for 5 min at 4°C. The cell pellet was
763 resuspended in a mix of 22.5 µL FACS buffer and 2.5 µL of FcX (Biolegend; #422302) and
764 incubated for 10 min at room temperature. After blocking, 25 µL of antibody cocktail targeting
765 hCD3, hCD20, hCD16, hHLA-DR, hCD45, hCD8, hCD4, hCD33, hCD45RA, hCD56, hCD14,
766 mCD45, and containing a LIVE/DEAD viability dye (ThermoFisher Scientific) was added to each
767 sample and incubated in the dark for 30 min at 4°C. After staining, 1 mL of FACS buffer was
768 added to each sample, samples were centrifuged at 300 x g for 5 min, washed with 1 mL FACS
769 buffer, centrifuged at 300 x g for 5 min, and then fixed in 200 µL 4% PFA for 30 min. After fixation
770 cells were washed twice with 1 mL FACS buffer, resuspended in FACS buffer, and stored
771 protected from light at 4°C until analysis. Human immune cell subsets were gated as follows:
772 human CD45+, hCD45+ mCD45-; human CD3+, hCD45+ hCD3+; human CD4+, hCD45+ hCD3+
773 hCD4+; human CD8+, hCD45+ hCD3+ hCD8+.
774
775 ***Flow cytometry analysis.*** For all flow cytometry experiments, flow cytometric analysis was
776 performed using an LSRII Flow Cytometer (BD Biosciences) or Cytek Aurora instrument (Cytek

777 Biosciences). Flow cytometry fluorophore compensation for antibodies was performed using an
778 AbC™ Anti-Mouse Bead Kit (ThermoFisher Scientific). Flow cytometry data were analyzed using
779 FlowJo software (TreeStar, Ashland, OR, USA).
780
781 ***Histologic processing and analysis.*** Tissue samples were fixed for 72 h in 10% neutral buffered
782 formalin, processed in a Tissue-Tek VIP-5 automated vacuum infiltration processor (Sakura
783 Finetek USA, Torrance, CA, USA), followed by paraffin embedding using a HistoCore Arcadia
784 paraffin embedding station (Leica, Wetzlar, Germany). Generated formalin-fixed, paraffin-
785 embedded (FFPE) blocks were sectioned to 5 µm using a RM2255 rotary microtome (Leica),
786 transferred to positively charged slides, deparaffinized in xylene, and dehydrated in graded
787 ethanol. Tissue sections were stained with hematoxylin and eosin for histologic examination, while
788 unstained slides were used for immunohistochemistry. Qualitative and semi-quantitative
789 histomorphological analyses were performed by a single board-certified veterinary pathologist
790 (N.A.C.). An ordinal scoring system was developed to capture the heterogeneity of histologic
791 findings in fLX. Individual histologic findings that were scored included: syncytial cells, hyaline
792 membranes, intra-airspace neutrophils and necrosis, hemorrhage, edema, denuded
793 pneumocytes, capillary fibrin thrombi, intermediate vessel fibrin thrombi and coagulative necrosis.
794 The entire fLX was examined at 200x with a DM2500 light microscope (Leica) using the following
795 criteria: 0 = not present, 1 = found in <5% of fields, 2 = found in >5% but <25% of fields, or 3 =
796 found in >25% of fields. Several criteria were also restricted to 'not observed' (0) or 'observed'
797 (1). Scores were combined to generate a cumulative lung injury score.
798
799 ***Histological Antibodies.*** The following primary antibodies from Cell Signaling Technology
800 (Danvers, MA, USA) were used: rabbit anti-human/mouse PAPRg (clone C26H12), rabbit anti-
801 human CD4 (clone EP204), rabbit anti-human CD163 (clone D6U1J), rabbit anti-human CD3e
802 (clone D7A6E), mouse anti-MHC class I (clone EMR8-5), and mouse anti-SARS-CoV-2 Spike (S)

803 (clone E7U6O/2B3E5]). The secondary antibody used in this study included HRP Goat anti-Rabbit
804 IgG (H&L) (Vector Laboratories, Burligame, CA, USA). For mouse derived primary antibodies, a
805 linker antibody (Abcam) was used prior to application of the secondary antibody to prevent non-
806 specific binding. DAB chromogen (Roche) and chromogens used for TSA-conjugated Opal 480,
807 520, 570, and 620 fluorophores (Akoya Biosciences, Marlborough, MA, USA) were utilized to
808 develop immunohistochemical assays. The following anti-SARS-CoV-2 antibodies were used for
809 immunohistochemistry: rabbit polyclonal anti-SARS-CoV Nucleoprotein (Novus Biological,
810 Littleton, CO, USA), mouse monoclonal anti-SARS-CoV-2 Spike clone 2B3E5 (This antibody was
811 used in this study as clone E7U60, which was the pre-production clone ID of clone 2B3E5; Cell
812 Signaling Technology).
813
814 ***Multispectral fluorescent imaging.*** Fluorescently labeled slides were imaged using either a
815 Mantra 2.0TMor Vectra Polaris TM Quantitative Pathology Imaging System (Akoya Biosciences).
816 To maximize signal-to-noise ratios, fluorescently acquired images were spectrally unmixed using
817 a synthetic library specific for the Opal fluorophores used in each assay plus DAPI. An unstained
818 fLX section was used to create an autofluorescence signature that was subsequently removed
819 from multispectral images using InForm software version 2.4.8 (Akoya Biosciences).
820
821 ***Transmission electron microscopy.*** Tissue samples were fixed for 72 h in a mixture of 2.5%
822 glutaraldehyde and 2% formaldehyde in 0.1 M sodium cacodylate buffer (pH 7.4). Samples were
823 then washed in 0.1 M cacodylate buffer and postfixed with 1% osmiumtetroxide (OsO4)/1.5%
824 potassiumferrocyanide (KFeCN6) for 1 h at room temperature. After washes in water and 50 mM
825 maleate buffer pH 5.15 (MB), the samples were incubated in 1% uranyl acetate in MB for 1 h,
826 washed in MB and water, and dehydrated in grades of alcohol (10 min each: 50%, 70%, 90%,
827 2x10 min 100%). The tissue samples were then put in propyleneoxide for 1 h and infiltrated
828 overnight in a 1:1 mixture of propyleneoxide and TAAB Epon. The following day the samples were

829 embedded in fresh TAAB Epon and polymerized at 60°C for 48 h. Semi-thin (0.5 μm) and ultrathin
830 sections (50-80 nm) were cut on a Reichert Ultracut-S microtome (Leica). Semi-thin sections were
831 picked up on glass slides and stained with toluidine blue for examination by light microscopy to
832 find affected areas in the tissue. Ultrathin sections from those areas were picked up onto
833 formvar/carbon coated copper grids, stained with 0.2% lead citrate and examined in a JEOL
834 1200EX transmission electron microscope (JOEL, Akishima, Tokyo, Japan). Images were
835 recorded with an AMT 2k CCD camera.
836
837 ***Bulk RNA sequencing.*** Total RNA was processed from fLX as described above, and sent to BGI
838 genomics (Hong Kong, China) for library preparation and sequencing (Pair-ends, 100 bp, 20M
839 reads per sample). Raw FASTQ files were quality-checked with FastQC v0.11.7. Reads were
840 found to be excellent quality and were aligned to the combined human (GRCh38, Ensembl 101)
841 and mouse (GRCm38, Ensembl 101) genomes with STAR v2.7.1a (Dobin et al., 2013) followed
842 by quantification with featureCounts v1.6.2 (Liao et al., 2014). Quality was checked with MultiQC
843 v1.6. All samples passed quality thresholds of >75% sequences aligned and >15 million aligned
844 reads per sample. Significantly up- and downregulated genes were identified with DESeq2
845 v1.23.10 (Love et al., 2014) in R v3.6.0. Each post-infection timepoint was compared to naïve: 2
846 dpi vs. naïve, and 12 dpi vs. naïve. P-values were FDR-adjusted, and log2 fold change was shrunk
847 with the apeglm method. Significance was determined by an FDR-adjusted $p<0.01$ and a
848 shrunken log2 fold change>2 or <-2. DESeq2 result were imported into Ingenuity Pathway
849 Analysis (IPA; Service curated by Qiagen; Access provided through the Boston University
850 Genome Science Institute) (Kramer et al., 2014), and a canonical pathway enrichment analysis
851 was performed using the default settings and the same differential expression thresholds as
852 before (shrunken log2 fold change>2 or <-2 and FDR-adjusted p-value<0.01).
853

854 ***Single cell barcoding and sequencing.*** Following fLX processing into single cell suspension as
855 described above, cells were frozen down in a 90% FBS (Bio-Techne, R&D systems) 10% DMSO
856 solution (ThermoFisher Scientific) and kept at -80°C. Four to five days following freezing, cells
857 were thawed, and viability was assessed using Trypan blue (Fisher Scientific). Samples with
858 ≥90% viability were then processed using the Chromium Next GEM Single Cell 3' GEM, Library
859 & Gel Bead Kit v3.1, as per manufacturer instructions, and single cell barcoding was performed
860 using a Chromium instrument (10x genomics) located in the NEIDL BSL-3. Reverse transcription
861 of RNAs was performed in the BSL-3 using a thermocycler (Applied Biosciences), and cDNA was
862 then removed from containment. Full-length, barcoded cDNAs were then amplified by PCR to
863 generate sufficient mass for library construction. Enzyme fragmentation, A tailing, adaptor ligation
864 and PCR were then performed at the Boston University single-cell sequencing core to obtain final
865 libraries containing P5 and P7 primers used in Illumina bridge amplification. Size distribution and
866 molarity of resulting cDNA libraries were assessed via Bioanalyzer High Sensitivity DNA Assay
867 (Agilent Technologies, USA). All cDNA libraries were sequenced on an Illumina NextSeq 500
868 instrument at the Boston University microarray and sequencing core according to Illumina and
869 10x Genomics guidelines with 1.4-1.8pM input and 1% PhiX control library spike-in (Illumina,
870 USA).
871
872 ***Single-cell RNA sequencing analysis.***
873 Sequencing data was processed via 10X Genomics Cell Ranger 6.0.2. A custom reference was
874 built from the combined human (GRCh38, Ensembl 101) and mouse (GRCm38, Ensembl 101)
875 genomes. FASTQ files were generated from raw Illumina BCL files using *cellranger mkfastq*.
876 FASTQ files were aligned to the custom reference and quantified with *cellranger count*.
877 Quantification outputs were loaded and analyzed in R with the Seurat package (4.0.2, (Hao et al.,
878 2021)). Cells with nFeature_RNA between 200 and 7500, and MT.percent<= 50 were analyzed.
879 The dataset was normalized and scaled, and cell cycle scores (S+G2M) and nCount_RNA were

880 regressed. Seurat's RunPCA function was used to determine the number of PCA used for
881 subsequent analysis. FindClusters function was used to cluster cells. RunUMAP function was
882 used for UMAP visualization. A human score was calculated using all human genes, to
883 discriminate between mouse and human cells (**Fig. S3A-C**). Human cells were kept for
884 subsequent analysis. The following ("dimension";"resolution") parameters were used to cluster
885 the whole human dataset (15;0.1), epithelial cells (10;0.3), mesenchymal (10;0.4), endothelial
886 (10;0.5), T cell/ILC (12;0.4), and Myeloid cells (10;0.2). B cell, endothelial cell, epithelial cell,
887 mesenchymal cell, and mast cell clusters were identified by scoring using gene lists defined for
888 lung subsets in the COVID-19 atlas of ToppCell (**Fig. S3D**) (Jin et al., 2021). For chondrocytes,
889 which are not present in this dataset, we used the following gene list *ACAN, ITGA10, CYTL1,*
890 *HAPLN1, SNORC, COL2A1, COL9A2, COL11A2, SOX9, SOX6, ZBTB16, FOXC1, and GATA2*.
891 For T cells and ILC, a manually curated gene list based on ToppCell was used. Consensus
892 signature genes from LGEA LungMAP (Sun et al., 2022b) were used to validate each cluster.
893 Differentially expressed genes between clusters and conditions were identified using
894 FindMarkers. Only genes showing expression in at least 10% of cells in one of the groups
895 compared, p_val_adj < 0.05, and abs(fold change)>2 were considered.
896
897 ***Sequencing of SARS-CoV-2 virus from fLX.*** Viral sequences were amplified using a modified
898 version of the ARTIC3 tiled amplicon sequencing protocol (Quick 2020, Tyson 2020) and
899 sequenced on an Illumina MiSeq V3 600 cycle kit. Briefly, viral RNA was extracted from serum
900 using X protocol (I don't know the details). cDNA was synthesized from the viral RNA using a mix
901 of random hexamer and oligo-dT primers (IDT) and SSIV reverse transcriptase (Thermo Fisher).
902 Tiled amplicons were amplified using Q5 Hot Start polymerase (NEB) and the pooled primers
903 described in ARTIC3 (Quick 2020, Tyson 2020). Illumina sequencing adaptors were ligated onto
904 the amplicons using the NEBNext Adaptor kit for Illumina (NEB). The amplicons were then pooled,
905 cleaned up, and size selected using AMPureXP beads (Beckman Coulter). The pooled library

906 was quantified using Tape Station (Agilent) and Qbit (Thermo Fisher) kits. The library was
907 sequenced on a MiSeq with a V3 600 cycle kit (Illumina). Sequencing reads were filtered, trimmed,
908 and mapped to the D-WA reference sequence (Geneious). Variants were called using the
909 Geneious variant caller, with a minimum frequency threshold of 25%. Each positive variant was
910 visually inspected.
911
912 ***Quantification and statistical Analysis.*** For histopathological score, viral loads/titers
913 comparison and Spike quantification, Kruskal-Wallis, Kolmogorov-Smirnov non-parametric t-test,
914 or a two-way ANOVA with Benjamini, Krieger, and Yekutieli correction for multiple comparisons
915 were applied given the non-continuous nature of the data (i.e., viral inoculation in areas displaying
916 differential stage of tissue development, and/or differences in fLX engraftment, and/or
917 donor/gestational age differences). A two-way ANOVA with Benjamini, Krieger, and Yekutieli
918 correction for multiple comparisons was also used to generate the ISG p.value heatmap given
919 the non-parametric nature of these data. For quantitative analysis of hematopoietic cell infiltration
920 (i.e. multiplex IHC and flowcytometry data), Welch's t-test or one-way ANOVA tests were used.
921 For comparison of viral gene count between macrophage clusters and other clusters, a Mann-
922 Whitney t-test was used. All statistical tests and graphical depictions of results were performed
923 using GraphPad Prism version 9.0.1 software (GraphPad Software, La Jolla, CA). For all tests,
924 $p \leq 0.05$ was considered statistically significant. Statistical significance on figures and
925 supplemental figures is labelled as follow: *$p \leq 0.05$, **$p \leq 0.01$, ***$p \leq 0.001$, ****$p \leq 0.0001$.
926
927 ***Data availability***. The accession number for the raw data of the bulk and single-cell RNA-Seq is
928 GSE255200.
929
930
931

932 **ACKNOWLEDGMENTS**

933 This work was supported in part by a start-up fund and Peter Paul Career Development
934 Professorship from Boston University (to F.D.), grants from the National Institutes of Health (K22
935 AI144050 to F.D.), Clinical and Translational Science Awards (grant UL1 TR001430) from the
936 National Center for Advancing Translational Sciences of the National Institutes of Health (to F.D.,
937 N.A.C. and A.E.), and an Evergrande MassCPR award (to R.B.). A.B.B. was supported by
938 R01AI174875, R01AI174276, DP2DA040254, as well as CDC subcontract 200-2016-91773-
939 T.O.2. and a Massachusetts Consortium on Pathogenesis Readiness (MassCPR) grant. We also
940 thank the Evans Center for Interdisciplinary Biomedical Research at Boston University Chobanian
941 and Avedisian School of Medicine for their support of the Affinity Research Collaborative on
942 'Respiratory Viruses: A Focus on COVID19'. This work utilized a Ventana Discovery Ultra and
943 Akoya PhenoImager HT that were purchased with funding from National Institutes of Health SIG
944 grants (S10 OD026983 & S10OD030269). We thank Ronald B. Corley, NEIDL director at the time
945 of this study and MassCPR award recipient, for his constant encouragement and support for this
946 study. We thank the Boston University Animal Science Center, the Ragon Institute Human
947 Immune System Mouse core, the single cell sequencing core and microarray and sequencing
948 core, and the flow cytometry core at Boston University Chobanian and Avedisian School of
949 Medicine, and all the NEIDL animal core staff for their outstanding support. We also thank all the
950 Douam, Balazs, Connor and Crossland lab members, NEIDL members, and members of the
951 department of virology, immunology, and microbiology and pathology at Boston University for
952 their constant support and advice. D.K. is supported by a T32 training grant in immunology
953 (T32AI007309). The authors have no conflicting financial interests.

954 Author contributions: D.K., A.B.B. and F.D. conceptualized the overall study. C.H.
955 conceptualized the computational component of this study and oversaw the analysis of the single-
956 cell RNA sequencing data. D.K., A.B.B., N.A.C. and F.D. designed the experiments. D.K., A.K.O.,
957 M.S, A.N, H.P.G., M.E., V.V., A.B.B. and F.D. performed experiments. D.K., A.K.O., A.T., J.T.,

958 M.S, A.N, P.M., M.E., J.H.C., V.V., N.A.C., C.H., A.B.B. and F.D. analyzed the data. J.T and C.H.
959 carried out computational analysis. M.E. carried out electron microscopy analysis. A.B.B. and V.V.
960 provided access to key resources. D.K. and F.D. wrote the manuscript with contributions from all
961 authors.
962
963 **FIGURE LEGENDS**
964 **Figure 1. BLT-L mice effectively resolve SARS-CoV-2 infection and repair lung tissue.** Fetal
965 lung xenografts (fLX) of BLT-L mice were infected with $1x10^6$ PFU of SARS-CoV-2 WA-1 isolate
966 via subcutaneous intra-graft injection. **(A)** BLT-L mice were monitored for weight change over the
967 course of 12-days post infection (dpi). **(B)** Immunohistochemistry for SARS-CoV-2 S protein **(a-**
968 **d)** and hematoxylin and eosin staining **(e-f)** were performed on naïve fLX **(a,e)** and fLX at 2 dpi
969 **(b,f)**, 6 dpi **(c,g),** and 12 dpi **(d,h)**. Scale bar = 100 μM **(C)** Viral titer (log(PFU/mg)) in fLX at 2, 6,
970 and 12 dpi as determined by plaque assay. **(D)** Histopathological scoring of naïve fLX and fLX at
971 2, 6, and 12 dpi. Data are representative of two or three independent experiments. n = 6 -10 per
972 timepoint. Error bars represent mean ± standard error of the mean (SEM). *One-way ANOVA*
973 *analysis was performed. p-values are indicated on graphs and only significant comparisons are*
974 *shown.*
975
976 **Figure 2**. **Cellular remodeling and viral dynamics in fLX upon SARS-CoV-2 infection**
977 Single cell RNA sequencing analysis was performed on single cell suspensions of naïve fLX and
978 fLX at 2 and 12 dpi. Naïve n=3 fLX (9,605 cells), 2 dpi n=2 fLX (4,405 cells), and 12 dpi n = 2 fLX
979 (5,857 cells). **(A)** UMAP plot clustering of the human cell compartment of naïve fLX and fLX at 2
980 and 12 dpi. **(B)** Temporal annotation of the human clusters on the UMAP plot: naïve (black), 2 dpi
981 (red), 12 dpi (blue). Clusters unique to 2 dpi are annotated by A (T cell compartment), B
982 (mesenchymal compartment), or C (myeloid compartment). **(C)** Frequency of each cell
983 compartment determined by single cell RNA-sequencing. **(D)** Dot plots displaying the expression

984 of SARS-CoV-2 viral RNA transcripts identified in scRNA-seq. **(E)** UMAP plot showing the
985 distribution of SARS-CoV-2 viral RNA transcripts across all human cell clusters and time points.
986 **(F)** UMAP plot sub-clustering of the human epithelial compartment of fLX across all time points.
987 **(G)** Temporal annotation of the human epithelial sub-clusters on the UMAP plot: naïve (black), 2
988 dpi (red), 12 dpi (blue). The inset graph indicates the change in frequency of each compartment
989 (AT2; black, Basal; pink, Secretory; teal, and AT1; purple) within the epithelial compartment. Red
990 line indicates the change in the AT2 compartment over time. **(H)** Heatmap displaying the relative
991 expression (from -1 to 1) of the top differentially regulated genes over the course of infection within
992 the AT2 compartment.
993
994 **Figure 3. A unique T-cell subset is enriched for viral RNA and specific for 2 dpi. (A)** UMAP
995 plot showing the sub-clustering of the human T-cell compartment of fLX across all time points.
996 **(B)** Temporal annotation of the human T-cell sub-clusters on the UMAP plot: naïve (black), 2 dpi
997 (red), 12 dpi (blue). **(C)** UMAP plot (all time points) showing the distribution of SARS-CoV-2 viral
998 RNA transcripts in the T-cell compartment. **(D)** Go-term analysis showing the most highly
999 upregulated signaling pathways in the macrophage-like T-cell cluster (cluster 6). **(E)** Relative
1000 expression of T-cells, macrophage, mesenchymal and antiviral markers within each of the T-cell
1001 sub-clusters (From 0 to 8; as labeled in panel A.).
1002
1003 **Figure 4. CD163+ inflammatory monocytes arise during acute viral infection and are**
1004 **predominant antiviral mediators. (A)** UMAP plot showing sub-clustering of the human myeloid
1005 compartment of fLX across all time points. **(B)** Temporal annotation of the myeloid sub-clusters
1006 on the UMAP plot: naïve (black), 2 dpi (red), 12 dpi (blue). iMO cluster is indicated with a blue
1007 circle. **(C)** UMAP plot (all time points) showing the distribution of SARS-CoV-2 viral RNA
1008 transcripts in the myeloid compartment. **(D-F)** UMAP plot showing the expression of CD*163* **(D),**
1009 *CD4* **(E)**, and *MRC1* **(F)** across myeloid sub-sets. **(G)** Frequency of each myeloid sub-cluster by

1010 timepoint. **(H)** Relative expression of highly upregulated ISGs and inflammatory markers in each
1011 of the myeloid sub-clusters. **(I)** Multiplex fluorescent immunohistochemistry of naïve fLX and fLX
1012 at 2 and 12 dpi. CD163: teal, CD4: yellow, CD3: orange, PPARγ: green, Dapi: gray. Two
1013 representative images. Scale bar = 100 μM **(J)** Violin plots showing expression level of
1014 differentially expressed genes between SARS-CoV-2 positive and negative iMo (cluster 3).
1015
1016 **Figure 5. Loss of CD4+ monocytes results in persistent infection. (A)** BLT-L mice were
1017 administered 200 μg of anti-CD3e (OKT3), anti-CD4 (OKT4), anti-CD8 (OKT8) or IgG2a isotype.
1018 **(B)** Viral titer (log(PFU/mg)) in fLX extracted from BLT-L mice treated with isotype, OKT3, OKT4,
1019 or OKT8 antibody at 12 dpi. **(C)** MHC-I staining of fLX tissue sections (anti-MHC class I (EMR8-
1020 5) CST 88274) extracted from naïve mice, OKT4-treated mice (12 dpi), or from infected fLX at 2
1021 and 12 dpi. Scale bar = 100 μM **(D^{a-g})** Multiplex immunohistochemistry of fLX tissue sections
1022 extracted from Isotype (a), OKT3 (b,c), OKT4 (d,e), or OKT8 (f,g)-treated BLT-L mice at 12 dpi.
1023 CD163: teal, CD4: yellow, CD3: orange, PPARγ: green, Dapi: gray. Viral titer (PFU/mg) of the
1024 respective fLX is inlaid in white. Scale bar = 100 μM **(E-H)** Quantification of selected cytokines
1025 (CCL2, CCL3, CXCL10 and CCL19) in the serum of naïve and infected BLT-L mice (2 dpi or 12
1026 dpi), and of OKT4-treated BLT-L mice (12 dpi). **(I)** Histopathological scoring of fLX extracted from
1027 isotype, OKT3, OKT4, or OKT8-treated BLT-L mice. One-*way ANOVA. p-values are indicated on*
1028 *graphs. Error bars indicate mean ± Standard error of the mean.*
1029
1030 **Figure 6. The non-hematopoietic compartment of BLT-L fLX respond to infection and**
1031 **promote immune recruitment and tissue repair. (A)** UMAP plot sub-clustering of the human
1032 mesenchymal compartment of fLX across all time points. **(B)** Temporal annotation of the
1033 mesenchymal sub-clusters on the UMAP plot: naïve (black), 2 dpi (red), 12 dpi (blue). **(C)**
1034 Frequency of each mesenchymal sub-cluster within the entire mesenchymal compartment over

1035 the course of infection. Each cluster ID is labelled as in Panel A. **(D)** Heatmap displaying the
1036 relative expression of top differentially regulated genes over the course of infection within the
1037 activated fibroblast sub-cluster (Cluster 3). **(E)** Go-term analysis showing the most highly
1038 upregulated signaling pathways in the activated fibroblast sub-cluster (Cluster 3). **(F-G)** UMAP
1039 plot showing the expression of *CXCL10* **(F)** and *TIMP1* **(G)** in the mesenchymal compartment and
1040 across all time points. **(H)** UMAP plot sub-clustering of the human endothelial compartment of fLX
1041 across all time points. **(I)** Temporal annotation of the endothelial sub-clusters on the UMAP plot:
1042 naïve (black), 2 dpi (red), 12 dpi (blue). **(J)** List of upregulated (red) and downregulated (blue)
1043 genes specific to the activated endothelial sub-cluster (Cluster 2) over the other endothelial sub-
1044 clusters (*p.adj*≤0.05). **(K)** Heatmap displaying the relative expression of the top differentially
1045 regulated genes over the course of infection within the venous endothelial sub-cluster (Cluster 0).
1046
1047 **Figure 7. Immunological events defining the successful resolution of SARS-CoV-2**
1048 **infection in human lung tissues.**
1049
1050 **SUPPLEMENTAL FIGURE LEGENDS**
1051 **Figure S1. BLT-L mice are susceptible to SARS-CoV-2 infection and display with**
1052 **transcriptomic changes at 2 and 12 dpi. (A-D)** Transmission electron microscopy (TEM) of fLX
1053 tissue sections extracted from BLT-L mice at 2 dpi illustrating virus particles in AT2 cells as evident
1054 by presence of lamellar bodies. Scale bars indicated on image. **(E)** Neutralizing efficacy (ND50
1055 values) of serum extracted from naïve or infected mice BLT-L mice (2 and 12 dpi). Assay was
1056 performed using VeroE6 cells and a recombinant WA-1 SARS-CoV-2 virus expressing NanoLuc.
1057 **(F)** Titration of the neutralizing activity of an anti-RBD antibody (serving as positive control)
1058 against WA-1 SARS-CoV-2 virus expressing NanoLuc. **(G-I)** SARS-Cov-2 attributable
1059 histopathology in BLT-L fLX at 2 dpi. **(G)** Bronchiolar attenuation and denuding (blue arrows)
1060 correlates directly with the presence of SARS-CoV-2 Spike protein. **(H)** Alveolar spaces are

1061 multifocally filled with necrotic debris admixed with neutrophils and edema (blue hashes). Type II
1062 pneumocytes (ATII) are often denuded or attenuated in areas of inflammation that correlates
1063 directly with the presence of SARS-CoV-2 Spike protein. Fibrin thrombi are routinely observed in
1064 neighboring parenchyma (black asterisks). **(I)** Coagulative necrosis as evidenced by loss of
1065 cellular detail and generalized eosinophilia (above the black hashed line) with numerous regional
1066 fibrin thrombi (black asterisks). Although SARS-CoV-2 Spike protein is not observed in the area
1067 of coagulative necrosis viral antigen is located within adjacent tissue. **(J-N)** Bulk RNA-sequencing
1068 analysis was performed on total RNA extracted from fLX of naïve (n=4) or infected BLT-L mice at
1069 2 (n=4) and 12 dpi (n=3). **(J)** Sequencing reads were aligned to a combined mouse (white), human
1070 (black) and SARS-CoV-2 viral (red) genome. Samples containing greater than 60% human reads
1071 (red dotted line) were included for analysis. **(K)** PCA plot showing clustering of naïve (black), 2-
1072 (green) and 12 dpi (purple) samples. **(L)** Significantly differentially expressed genes (*p.adj*≤0.05;
1073 upregulated: red, downregulated: blue) at 2- and 12 dpi. **(M)** Venn diagram showing the overlap
1074 of upregulated (left) and downregulated (right) genes between 2- and 12 dpi. **(N)** Volcano plot
1075 showing significantly downregulated (blue) and upregulated (red) genes at 2- and 12 dpi.
1076

1077 **Figure S2. Single-cell RNA sequencing analysis of fLX upon SARS-CoV-2 infection. (A-E)**
1078 Single cell RNA sequencing was performed on naïve fLX and infected fLX (at 2- and 12 dpi).
1079 Sequencing reads were aligned to a combined human, mouse and SARS-CoV-2 viral genome.
1080 **(A)** UMAP plot clustering on all cell (human and mouse) populations detected. **(B)** Expression of
1081 mouse (top) and human *GAPDH* (bottom) in all clusters. **(C)** A human score was applied to each
1082 cluster to identify human clusters (above dotted line) and mouse clusters (below dotted line; gray
1083 zone). Mouse clusters were removed from downstream analysis. **(D)** Cell scoring system applied
1084 to human cell clusters to classify each cluster. **(E)** Flow cytometric analysis showing frequency of
1085 hCD45+, hCD3+, hCD4+, and hCD8+ cells among PBMCs extracted from the blood of naïve and

1086 infected BLT-L mice at 2-, 6-, and 12 dpi. **(F)** UMAP clustering of human cells separated by time
1087 point (naïve: left, 2 dpi: center, and 12 dpi: right).
1088
1089 **Figure S3. Gene signature of macrophage-like T cells. (A)** UMAP showing viral RNA reads
1090 across all human clusters. The mesenchymal cluster is enlarged. **(B)** Mitochondrial gene
1091 expression among the different T cell sub-clusters. **(C)** Expression of T-cell associated genes
1092 among the different T-cell sub-clusters. **(D)** Expression of myeloid/macrophage-associated genes
1093 among the different T-cell sub-clusters.
1094
1095 **Figure S4. Gene signature of myeloid and inflammatory monocytes sub-clusters. (A-C)**
1096 Violin plot displaying monocyte **(A)**, macrophage **(B)** and dendritic cell **(C)** gene signature score
1097 for each myeloid sub-cluster. **(D)** UMAP plots representing the expression of several myeloid
1098 markers that were employed to further define the identity of the different myeloid sub-clusters.
1099
1100 **Figure S5. Hematopoietic subset depletion in BLT-L mice and myeloid chemotaxis in**
1101 **infected fLX. (A)** Flow cytometric analysis showing the frequency of hCD45+, hCD3+, hCD3+
1102 hCD4+, and hCD3+ hCD8+ cells among PBMCs extracted from the blood of BLT-L mice treated
1103 with an isotype antibody, OKT3, OKT4 or OKT8 antibody. *One-way ANOVA. P-value indicated*
1104 *on graph. Error bars represent mean ± SEM.* **(B-C)** UMAP plots showing the
1105 compartmentalization of *CCL2* **(B)** and *CCL3* **(C)** expression within all human cell populations in
1106 naïve or infected (2 and 12 dpi) fLX. **(D)** List of additional downregulated genes specific to the
1107 activated endothelial sub-cluster (Cluster 2) over the other endothelial sub-clusters (*p.adj*≤0.05).
1108 **(E,F)** UMAP plot showing the expression of *INSR* **(E)** and *CXCR4* **(F)** among all human
1109 endothelial sub-clusters. **(H)** Viral titer (log(PFU/mg)) of CD3 depleted (OKT3) and CD4 depleted
1110 (OKT4) fLX that were positive for infection. *Unpaired, non-parametric T-test. P-value indicated on*
1111 *graph.*

1112 **SUPPLEMENTAL MATERIALS**

1113 **Table S1.** SARS-CoV-2 mutations identified among viral reads isolated from fLX at 2 dpi and from
1114 our concentrated viral stock (i.e., WA1 positive stock used to inoculate fLX), as compared to the
1115 Wuhan-1 consensus sequence.

1116 **Data S1.** List of up- and down-regulated human genes in SARS-CoV-2-infected fLX at 2 and 12
1117 dpi using bulk RNA sequencing analysis.

1118

1119 **REFERENCES**

1120 Abe, T., T. Ikeda, Y. Tokuda, J. Ito, Y. Suzuki, C. Narahara, H. Iriyama, and K. Sato. 2021. A
1121 patient infected with SARS-CoV-2 over 100 days. *QJM*. 114:47-49.
1122 Arshad, N., M. Laurent-Rolle, W.S. Ahmed, J.C. Hsu, S.M. Mitchell, J. Pawlak, D. Sengupta, K.H.
1123 Biswas, and P. Cresswell. 2023. SARS-CoV-2 accessory proteins ORF7a and ORF3a use
1124 distinct mechanisms to down-regulate MHC-I surface expression. *Proc Natl Acad Sci U S*
1125 *A*. 120:e2208525120.
1126 Augusto, D.G., L.D. Murdolo, D.S.M. Chatzileontiadou, J.J. Sabatino, Jr., T. Yusufali, N.D.
1127 Peyser, X. Butcher, K. Kizer, K. Guthrie, V.W. Murray, V. Pae, S. Sarvadhavabhatla, F.
1128 Beltran, G.S. Gill, K.L. Lynch, C. Yun, C.T. Maguire, M.J. Peluso, R. Hoh, T.J. Henrich,
1129 S.G. Deeks, M. Davidson, S. Lu, S.A. Goldberg, J.D. Kelly, J.N. Martin, C.A. Vierra-Green,
1130 S.R. Spellman, D.J. Langton, M.J. Dewar-Oldis, C. Smith, P.J. Barnard, S. Lee, G.M.
1131 Marcus, J.E. Olgin, M.J. Pletcher, M. Maiers, S. Gras, and J.A. Hollenbach. 2023. A
1132 common allele of HLA is associated with asymptomatic SARS-CoV-2 infection. *Nature*.
1133 620:128-136.
1134 Boumaza, A., L. Gay, S. Mezouar, E. Bestion, A.B. Diallo, M. Michel, B. Desnues, D. Raoult, B.
1135 La Scola, P. Halfon, J. Vitte, D. Olive, and J.-L. Mege. 2021a. Monocytes and
1136 macrophages, targets of SARS-CoV-2: the clue for Covid-19 immunoparalysis. *The*
1137 *Journal of Infectious Diseases*.
1138 Boumaza, A., L. Gay, S. Mezouar, E. Bestion, A.B. Diallo, M. Michel, B. Desnues, D. Raoult, B.
1139 La Scola, P. Halfon, J. Vitte, D. Olive, and J.L. Mege. 2021b. Monocytes and
1140 Macrophages, Targets of Severe Acute Respiratory Syndrome Coronavirus 2: The Clue
1141 for Coronavirus Disease 2019 Immunoparalysis. *J Infect Dis*. 224:395-406.
1142 Chen, D.Y., N. Khan, B.J. Close, R.K. Goel, B. Blum, A.H. Tavares, D. Kenney, H.L. Conway,
1143 J.K. Ewoldt, V.C. Chitalia, N.A. Crossland, C.S. Chen, D.N. Kotton, S.C. Baker, S.Y.
1144 Fuchs, J.H. Connor, F. Douam, A. Emili, and M. Saeed. 2021. SARS-CoV-2 disrupts
1145 proximal elements in the JAK-STAT pathway. *J Virol*:JVI0086221.
1146 Clayton, S.A., K.K. Daley, L. MacDonald, E. Fernandez-Vizarra, G. Bottegoni, J.D. O'Neil, T.
1147 Major, D. Griffin, Q. Zhuang, A.B. Adewoye, K. Woolcock, S.W. Jones, C. Goodyear, A.
1148 Elmesmari, A. Filer, D.A. Tennant, S. Alivernini, C.D. Buckley, R.D.S. Pitceathly, M.
1149 Kurowska-Stolarska, and A.R. Clark. 2021. Inflammation causes remodeling of
1150 mitochondrial cytochrome c oxidase mediated by the bifunctional gene C15orf48. *Sci Adv*.
1151 7:eabl5182.
1152 Damas, J.K., L. Landro, B. Fevang, L. Heggelund, G.E. Tjonnfjord, Y. Floisand, B. Halvorsen,
1153 S.S. Froland, and P. Aukrust. 2009. Homeostatic chemokines CCL19 and CCL21 promote

1154 inflammation in human immunodeficiency virus-infected patients with ongoing viral
1155 replication. *Clin Exp Immunol*. 157:400-407.
1156 Delorey, T.M., C.G.K. Ziegler, G. Heimberg, R. Normand, Y. Yang, A. Segerstolpe, D.
1157 Abbondanza, S.J. Fleming, A. Subramanian, D.T. Montoro, K.A. Jagadeesh, K.K. Dey, P.
1158 Sen, M. Slyper, Y.H. Pita-Juarez, D. Phillips, J. Biermann, Z. Bloom-Ackermann, N.
1159 Barkas, A. Ganna, J. Gomez, J.C. Melms, I. Katsyv, E. Normandin, P. Naderi, Y.V. Popov,
1160 S.S. Raju, S. Niezen, L.T. Tsai, K.J. Siddle, M. Sud, V.M. Tran, S.K. Vellarikkal, Y. Wang,
1161 L. Amir-Zilberstein, D.S. Atri, J. Beechem, O.R. Brook, J. Chen, P. Divakar, P. Dorceus,
1162 J.M. Engreitz, A. Essene, D.M. Fitzgerald, R. Fropf, S. Gazal, J. Gould, J. Grzyb, T.
1163 Harvey, J. Hecht, T. Hether, J. Jane-Valbuena, M. Leney-Greene, H. Ma, C. McCabe,
1164 D.E. McLoughlin, E.M. Miller, C. Muus, M. Niemi, R. Padera, L. Pan, D. Pant, C. Pe'er, J.
1165 Pfiffner-Borges, C.J. Pinto, J. Plaisted, J. Reeves, M. Ross, M. Rudy, E.H. Rueckert, M.
1166 Siciliano, A. Sturm, E. Todres, A. Waghray, S. Warren, S. Zhang, D.R. Zollinger, L. Cosimi,
1167 R.M. Gupta, N. Hacohen, H. Hibshoosh, W. Hide, A.L. Price, J. Rajagopal, P.R. Tata, S.
1168 Riedel, G. Szabo, T.L. Tickle, P.T. Ellinor, D. Hung, P.C. Sabeti, R. Novak, R. Rogers,
1169 D.E. Ingber, Z.G. Jiang, D. Juric, M. Babadi, S.L. Farhi, B. Izar, J.R. Stone, et al. 2021a.
1170 COVID-19 tissue atlases reveal SARS-CoV-2 pathology and cellular targets. *Nature*.
1171 Delorey, T.M., C.G.K. Ziegler, G. Heimberg, R. Normand, Y. Yang, A. Segerstolpe, D.
1172 Abbondanza, S.J. Fleming, A. Subramanian, D.T. Montoro, K.A. Jagadeesh, K.K. Dey, P.
1173 Sen, M. Slyper, Y.H. Pita-Juárez, D. Phillips, Z. Bloom-Ackerman, N. Barkas, A. Ganna,
1174 J. Gomez, E. Normandin, P. Naderi, Y.V. Popov, S.S. Raju, S. Niezen, L.T.Y. Tsai, K.J.
1175 Siddle, M. Sud, V.M. Tran, S.K. Vellarikkal, L. Amir-Zilberstein, D.S. Atri, J. Beechem,
1176 O.R. Brook, J. Chen, P. Divakar, P. Dorceus, J.M. Engreitz, A. Essene, D.M. Fitzgerald,
1177 R. Fropf, S. Gazal, J. Gould, J. Grzyb, T. Harvey, J. Hecht, T. Hether, J. Jane-Valbuena,
1178 M. Leney-Greene, H. Ma, C. McCabe, D.E. McLoughlin, E.M. Miller, C. Muus, M. Niemi,
1179 R. Padera, L. Pan, D. Pant, C. Pe'er, J. Pfiffner-Borges, C.J. Pinto, J. Plaisted, J. Reeves,
1180 M. Ross, M. Rudy, E.H. Rueckert, M. Siciliano, A. Sturm, E. Todres, A. Waghray, S.
1181 Warren, S. Zhang, D.R. Zollinger, L. Cosimi, R.M. Gupta, N. Hacohen, W. Hide, A.L. Price,
1182 J. Rajagopal, P.R. Tata, S. Riedel, G. Szabo, T.L. Tickle, D. Hung, P.C. Sabeti, R. Novak,
1183 R. Rogers, D.E. Ingber, Z. Gordon Jiang, D. Juric, M. Babadi, S.L. Farhi, J.R. Stone, I.S.
1184 Vlachos, I.H. Solomon, O. Ashenberg, C.B.M. Porter, B. Li, A.K. Shalek, A.-C. Villani, et
1185 al. 2021b. A single-cell and spatial atlas of autopsy tissues reveals pathology and cellular
1186 targets of SARS-CoV-2. *bioRxiv*:2021.2002.2025.430130.
1187 Di, Y., J. Lew, U. Goncin, A. Radomska, S.S. Rout, B.E.T. Gray, S. Machtaler, D. Falzarano, and
1188 K.J. Lavender. 2022. SARS-CoV-2 Variant-Specific Infectivity and Immune Profiles Are
1189 Detectable in a Humanized Lung Mouse Model. *Viruses*. 14.
1190 Dobin, A., C.A. Davis, F. Schlesinger, J. Drenkow, C. Zaleski, S. Jha, P. Batut, M. Chaisson, and
1191 T.R. Gingeras. 2013. STAR: ultrafast universal RNA-seq aligner. *Bioinformatics*. 29:15-
1192 21.
1193 Edahiro, R., Y. Shirai, Y. Takeshima, S. Sakakibara, Y. Yamaguchi, T. Murakami, T. Morita, Y.
1194 Kato, Y.C. Liu, D. Motooka, Y. Naito, A. Takuwa, F. Sugihara, K. Tanaka, J.B. Wing, K.
1195 Sonehara, Y. Tomofuji, C.-T.F. Japan, H. Namkoong, H. Tanaka, H. Lee, K. Fukunaga,
1196 H. Hirata, Y. Takeda, D. Okuzaki, A. Kumanogoh, and Y. Okada. 2023. Single-cell
1197 analyses and host genetics highlight the role of innate immune cells in COVID-19 severity.
1198 *Nat Genet*. 55:753-767.
1199 Evren, E., E. Ringqvist, K.P. Tripathi, N. Sleiers, I.C. Rives, A. Alisjahbana, Y. Gao, D. Sarhan,
1200 T. Halle, C. Sorini, R. Lepzien, N. Marquardt, J. Michaelsson, A. Smed-Sorensen, J.
1201 Botling, M.C.I. Karlsson, E.J. Villablanca, and T. Willinger. 2021. Distinct developmental
1202 pathways from blood monocytes generate human lung macrophage diversity. *Immunity*.
1203 54:259-275 e257.

1204 Fagre, A., J. Lewis, M. Eckley, S. Zhan, S.M. Rocha, N.R. Sexton, B. Burke, B. Geiss, O. Peersen,
1205 T. Bass, R. Kading, J. Rovnak, G.D. Ebel, R.B. Tjalkens, T. Aboellail, and T. Schountz.
1206 2021. SARS-CoV-2 infection, neuropathogenesis and transmission among deer mice:
1207 Implications for spillback to New World rodents. *PLoS Pathog*. 17:e1009585.
1208 Fan, C., Y. Wu, X. Rui, Y. Yang, C. Ling, S. Liu, S. Liu, and Y. Wang. 2022. Animal models for
1209 COVID-19: advances, gaps and perspectives. *Signal transduction and targeted therapy*.
1210 7:220.
1211 Finkel, Y., A. Gluck, A. Nachshon, R. Winkler, T. Fisher, B. Rozman, O. Mizrahi, Y. Lubelsky, B.
1212 Zuckerman, B. Slobodin, Y. Yahalom-Ronen, H. Tamir, I. Ulitsky, T. Israely, N. Paran, M.
1213 Schwartz, and N. Stern-Ginossar. 2021. SARS-CoV-2 uses a multipronged strategy to
1214 impede host protein synthesis. *Nature*. 594:240-245.
1215 Fu, L., Z. Liu, and Y. Liu. 2023. Fibrinogen-like protein 2 in inflammatory diseases: A future
1216 therapeutic target. *Int Immunopharmacol*. 116:109799.
1217 Grant, R.A., L. Morales-Nebreda, N.S. Markov, S. Swaminathan, M. Querrey, E.R. Guzman, D.A.
1218 Abbott, H.K. Donnelly, A. Donayre, I.A. Goldberg, Z.M. Klug, N. Borkowski, Z. Lu, H.
1219 Kihshen, Y. Politanska, L. Sichizya, M. Kang, A. Shilatifard, C. Qi, J.W. Lomasney, A.C.
1220 Argento, J.M. Kruser, E.S. Malsin, C.O. Pickens, S.B. Smith, J.M. Walter, A.E. Pawlowski,
1221 D. Schneider, P. Nannapaneni, H. Abdala-Valencia, A. Bharat, C.J. Gottardi, G.R.S.
1222 Budinger, A.V. Misharin, B.D. Singer, R.G. Wunderink, R.A. Grant, L. Morales-Nebreda,
1223 N.S. Markov, S. Swaminathan, M. Querrey, E.R. Guzman, D.A. Abbott, H.K. Donnelly, A.
1224 Donayre, I.A. Goldberg, Z.M. Klug, N. Borkowski, Z. Lu, H. Kihshen, Y. Politanska, L.
1225 Sichizya, M. Kang, A. Shilatifard, C. Qi, J.W. Lomasney, A.C. Argento, J.M. Kruser, E.S.
1226 Malsin, C.O. Pickens, S.B. Smith, J.M. Walter, A.E. Pawlowski, D. Schneider, P.
1227 Nannapaneni, H. Abdala-Valencia, A. Bharat, C.J. Gottardi, G.R.S. Budinger, A.V.
1228 Misharin, B.D. Singer, R.G. Wunderink, A.A. Wagh, A.R. Hauser, A.R. Wolfe, A. Thakrar,
1229 A.V. Yeldandi, A.A. Wang, A.R. Levenson, A.M. Joudi, B. Tran, C.A. Gao, C. Kurihara,
1230 C.J. Schroedl, C.M. Horvath, D. Meza, D.D. Odell, D.W. Kamp, D.R. Winter, E.A. Ozer,
1231 E.D. Shanes, E.T. Bartom, E.J. Rendleman, E.M. Leibenguth, F. Wehbe, G.Y. Liu, G.T.
1232 Gadhvi, H.T. Navarro, J.I. Sznajder, J.E. Dematte, et al. 2021. Circuits between infected
1233 macrophages and T cells in SARS-CoV-2 pneumonia. *Nature*. 590:635-641.
1234 Gubernatorova, E.O., E.A. Gorshkova, A.I. Polinova, and M.S. Drutskaya. 2020. IL-6: Relevance
1235 for immunopathology of SARS-CoV-2. *Cytokine Growth Factor Rev*. 53:13-24.
1236 Gupta, S.K., P.G. Lysko, K. Pillarisetti, E. Ohlstein, and J.M. Stadel. 1998. Chemokine receptors
1237 in human endothelial cells. Functional expression of CXCR4 and its transcriptional
1238 regulation by inflammatory cytokines. *J Biol Chem*. 273:4282-4287.
1239 Hao, Y., S. Hao, E. Andersen-Nissen, W.M. Mauck, 3rd, S. Zheng, A. Butler, M.J. Lee, A.J. Wilk,
1240 C. Darby, M. Zager, P. Hoffman, M. Stoeckius, E. Papalexi, E.P. Mimitou, J. Jain, A.
1241 Srivastava, T. Stuart, L.M. Fleming, B. Yeung, A.J. Rogers, J.M. McElrath, C.A. Blish, R.
1242 Gottardo, P. Smibert, and R. Satija. 2021. Integrated analysis of multimodal single-cell
1243 data. *Cell*. 184:3573-3587 e3529.
1244 Hettle, D., S. Hutchings, P. Muir, E. Moran, and C.-G.U. consortium. 2022. Persistent SARS-CoV-
1245 2 infection in immunocompromised patients facilitates rapid viral evolution: Retrospective
1246 cohort study and literature review. *Clin Infect Pract*. 16:100210.
1247 Jin, K., E.E. Bardes, A. Mitelpunkt, J.Y. Wang, S. Bhatnagar, S. Sengupta, D.P. Krummel, M.E.
1248 Rothenberg, and B.J. Aronow. 2021. Implicating Gene and Cell Networks Responsible for
1249 Differential COVID-19 Host Responses via an Interactive Single Cell Web Portal.
1250 *bioRxiv*:2021.2006.2007.447287.
1251 Junqueira, C., A. Crespo, S. Ranjbar, L.B. de Lacerda, M. Lewandrowski, J. Ingber, B. Parry, S.
1252 Ravid, S. Clark, M.R. Schrimpf, F. Ho, C. Beakes, J. Margolin, N. Russell, K. Kays, J.
1253 Boucau, U. Das Adhikari, S.M. Vora, V. Leger, L. Gehrke, L.A. Henderson, E. Janssen,
1254 D. Kwon, C. Sander, J. Abraham, M.B. Goldberg, H. Wu, G. Mehta, S. Bell, A.E. Goldfeld,

1255 M.R. Filbin, and J. Lieberman. 2022. FcgammaR-mediated SARS-CoV-2 infection of
1256 monocytes activates inflammation. *Nature*. 606:576-584.
1257 Kadiyska, T., I. Tourtourikov, K. Dabchev, R. Cherneva, N. Stoynev, R. Hadjiolova, V. Mitev, D.A.
1258 Spandidos, M. Adamaki, and V. Zoumpourlis. 2022. Role of endothelial dysfunction in the
1259 severity of COVID-19 infection (Review). *Molecular medicine reports*. 26.
1260 Kang, J.G., M.J. Amar, A.T. Remaley, J. Kwon, P.J. Blackshear, P.Y. Wang, and P.M. Hwang.
1261 2011. Zinc finger protein tristetraprolin interacts with CCL3 mRNA and regulates tissue
1262 inflammation. *J Immunol*. 187:2696-2701.
1263 Kenney, D.J., A.K. O'Connell, J. Turcinovic, P. Montanaro, R.M. Hekman, T. Tamura, A.R.
1264 Berneshawi, T.R. Cafiero, S. Al Abdullatif, B. Blum, S.I. Goldstein, B.L. Heller, H.P. Gertje,
1265 E. Bullitt, A.J. Trachtenberg, E. Chavez, E.T. Nono, C. Morrison, A.E. Tseng, A. Sheikh,
1266 S. Kurnick, K. Grosz, M. Bosmann, M. Ericsson, B.R. Huber, M. Saeed, A.B. Balazs, K.P.
1267 Francis, A. Klose, N. Paragas, J.D. Campbell, J.H. Connor, A. Emili, N.A. Crossland, A.
1268 Ploss, and F. Douam. 2022. Humanized mice reveal a macrophage-enriched gene
1269 signature defining human lung tissue protection during SARS-CoV-2 infection. *Cell Rep*.
1270 39:110714.
1271 Kohout, T.A., S.L. Nicholas, S.J. Perry, G. Reinhart, S. Junger, and R.S. Struthers. 2004.
1272 Differential desensitization, receptor phosphorylation, beta-arrestin recruitment, and
1273 ERK1/2 activation by the two endogenous ligands for the CC chemokine receptor 7. *J Biol*
1274 *Chem*. 279:23214-23222.
1275 Kosyreva, A., D. Dzhalilova, A. Lokhonina, P. Vishnyakova, and T. Fatkhudinov. 2021. The Role
1276 of Macrophages in the Pathogenesis of SARS-CoV-2-Associated Acute Respiratory
1277 Distress Syndrome. *Frontiers in Immunology*. 12.
1278 Lebedev, M., B. Faburay, J.A. Richt, and A. Young. 2021. Myeloid-like gammadelta T cell subset
1279 in the immune response to an experimental Rift Valley fever vaccine in sheep. *Vet*
1280 *Immunol Immunopathol*. 233:110184.
1281 Leroyer, A.S., M.G. Blin, R. Bachelier, N. Bardin, M. Blot-Chabaud, and F. Dignat-George. 2019.
1282 CD146 (Cluster of Differentiation 146). *Arterioscler Thromb Vasc Biol*. 39:1026-1033.
1283 Liao, Y., G.K. Smyth, and W. Shi. 2014. featureCounts: an efficient general purpose program for
1284 assigning sequence reads to genomic features. *Bioinformatics*. 30:923-930.
1285 Love, M.I., W. Huber, and S. Anders. 2014. Moderated estimation of fold change and dispersion
1286 for RNA-seq data with DESeq2. *Genome biology*. 15:550.
1287 Machkovech, H.M., A.M. Hahn, J. Garonzik Wang, N.D. Grubaugh, P.J. Halfmann, M.C. Johnson,
1288 J.E. Lemieux, D.H. O'Connor, A. Piantadosi, W. Wei, and T.C. Friedrich. 2024. Persistent
1289 SARS-CoV-2 infection: significance and implications. *Lancet Infect Dis*.
1290 Mao, G., Y. Kang, R. Lin, S. Hu, Z. Zhang, H. Li, W. Liao, and Z. Zhang. 2019. Long Non-coding
1291 RNA HOTTIP Promotes CCL3 Expression and Induces Cartilage Degradation by
1292 Sponging miR-455-3p. *Front Cell Dev Biol*. 7:161.
1293 Maponga, T.G., M. Jeffries, H. Tegally, A. Sutherland, E. Wilkinson, R.J. Lessells, N. Msomi, G.
1294 van Zyl, T. de Oliveira, and W. Preiser. 2023. Persistent Severe Acute Respiratory
1295 Syndrome Coronavirus 2 Infection With accumulation of mutations in a patient with poorly
1296 controlled Human Immunodeficiency Virus infection. *Clin Infect Dis*. 76:e522-e525.
1297 Molgora, M., and M. Colonna. 2022. Innate-like T cells: A promising asset in anti-cancer immunity.
1298 *Cancer Cell*. 40:714-716.
1299 Moriyama, M., C. Lucas, V.S. Monteiro, S.-C.-G.S.I. Yale, and A. Iwasaki. 2023. Enhanced
1300 inhibition of MHC-I expression by SARS-CoV-2 Omicron subvariants. *Proc Natl Acad Sci*
1301 *U S A*. 120:e2221652120.
1302 Munnur, D., Q. Teo, D. Eggermont, H.H.Y. Lee, F. Thery, J. Ho, S.W. van Leur, W.W.S. Ng, L.Y.L.
1303 Siu, A. Beling, H. Ploegh, A. Pinto-Fernandez, A. Damianou, B. Kessler, F. Impens, C.K.P.
1304 Mok, and S. Sanyal. 2021. Altered ISGylation drives aberrant macrophage-dependent
1305 immune responses during SARS-CoV-2 infection. *Nat Immunol*. 22:1416-1427.

1306 Muto, M., M. Baghdadi, R. Maekawa, H. Wada, and K. Seino. 2015. Myeloid molecular
1307 characteristics of human gammadelta T cells support their acquisition of tumor antigen-
1308 presenting capacity. *Cancer Immunol Immunother*. 64:941-949.
1309 Otifi, H.M., and B.K. Adiga. 2022. Endothelial Dysfunction in Covid-19 Infection. *Am J Med Sci*.
1310 363:281-287.
1311 Payankaulam, S., A.M. Raicu, and D.N. Arnosti. 2019. Transcriptional Regulation of INSR, the
1312 Insulin Receptor Gene. *Genes (Basel)*. 10.
1313 PMDA. 2021. Xevudy for Intravenous Infusion 500 mg_GlaxoSmithKline K.K._Report on Special
1314 Approval for Emergency; https://www.pmda.go.jp/files/000245006.pdf.
1315 Qian, Y., T. Lei, P.S. Patel, C.H. Lee, P. Monaghan-Nichols, H.B. Xin, J. Qiu, and M. Fu. 2021.
1316 Direct Activation of Endothelial Cells by SARS-CoV-2 Nucleocapsid Protein Is Blocked by
1317 Simvastatin. *J Virol*. 95:e0139621.
1318 Qin, Z., F. Liu, R. Blair, C. Wang, H. Yang, J. Mudd, J.M. Currey, N. Iwanaga, J. He, R. Mi, K.
1319 Han, C.C. Midkiff, M.A. Alam, B.H. Aktas, R.S.V. Heide, R. Veazey, G. Piedimonte, N.J.
1320 Maness, S. Ergun, F. Mauvais-Jarvis, J. Rappaport, J.K. Kolls, and X. Qin. 2021.
1321 Endothelial cell infection and dysfunction, immune activation in severe COVID-19.
1322 *Theranostics*. 11:8076-8091.
1323 Rathjen, T., B. Kunkemoeller, C.T. Cederquist, X. Wang, S.M. Lockhart, J.C. Patti, H. Willenbrock,
1324 G.S. Olsen, G.K. Povlsen, H.C. Beck, L.M. Rasmussen, Q. Li, K. Park, G.L. King, and C.
1325 Rask-Madsen. 2022. Endothelial Cell Insulin Signaling Regulates CXCR4 (C-X-C Motif
1326 Chemokine Receptor 4) and Limits Leukocyte Adhesion to Endothelium. *Arterioscler*
1327 *Thromb Vasc Biol*. 42:e217-e227.
1328 Ren, X., W. Wen, X. Fan, W. Hou, B. Su, P. Cai, J. Li, Y. Liu, F. Tang, F. Zhang, Y. Yang, J. He,
1329 W. Ma, J. He, P. Wang, Q. Cao, F. Chen, Y. Chen, X. Cheng, G. Deng, X. Deng, W. Ding,
1330 Y. Feng, R. Gan, C. Guo, W. Guo, S. He, C. Jiang, J. Liang, Y.M. Li, J. Lin, Y. Ling, H.
1331 Liu, J. Liu, N. Liu, S.Q. Liu, M. Luo, Q. Ma, Q. Song, W. Sun, G. Wang, F. Wang, Y. Wang,
1332 X. Wen, Q. Wu, G. Xu, X. Xie, X. Xiong, X. Xing, H. Xu, C. Yin, D. Yu, K. Yu, J. Yuan, B.
1333 Zhang, P. Zhang, T. Zhang, J. Zhao, P. Zhao, J. Zhou, W. Zhou, S. Zhong, X. Zhong, S.
1334 Zhang, L. Zhu, P. Zhu, B. Zou, J. Zou, Z. Zuo, F. Bai, X. Huang, P. Zhou, Q. Jiang, Z.
1335 Huang, J.X. Bei, L. Wei, X.W. Bian, X. Liu, T. Cheng, X. Li, P. Zhao, F.S. Wang, H. Wang,
1336 B. Su, Z. Zhang, K. Qu, X. Wang, J. Chen, R. Jin, and Z. Zhang. 2021. COVID-19 immune
1337 features revealed by a large-scale single-cell transcriptome atlas. *Cell*. 184:1895-1913
1338 e1819.
1339 Rendeiro, A.F., H. Ravichandran, Y. Bram, V. Chandar, J. Kim, C. Meydan, J. Park, J. Foox, T.
1340 Hether, S. Warren, Y. Kim, J. Reeves, S. Salvatore, C.E. Mason, E.C. Swanson, A.C.
1341 Borczuk, O. Elemento, and R.E. Schwartz. 2021. The spatial landscape of lung pathology
1342 during COVID-19 progression. *Nature*. 593:564-569.
1343 Schultze, J.L., and A.C. Aschenbrenner. 2021. COVID-19 and the human innate immune system.
1344 *Cell*. 184:1671-1692.
1345 Schyns, J., Q. Bai, C. Ruscitti, C. Radermecker, S. De Schepper, S. Chakarov, F. Farnir, D.
1346 Pirottin, F. Ginhoux, G. Boeckxstaens, F. Bureau, and T. Marichal. 2019. Non-classical
1347 tissue monocytes and two functionally distinct populations of interstitial macrophages
1348 populate the mouse lung. *Nat Commun*. 10:3964.
1349 Sefik, E., R. Qu, C. Junqueira, E. Kaffe, H. Mirza, J. Zhao, J.R. Brewer, A. Han, H.R. Steach, B.
1350 Israelow, H.N. Blackburn, S.E. Velazquez, Y.G. Chen, S. Halene, A. Iwasaki, E. Meffre,
1351 M. Nussenzweig, J. Lieberman, C.B. Wilen, Y. Kluger, and R.A. Flavell. 2022.
1352 Inflammasome activation in infected macrophages drives COVID-19 pathology. *Nature*.
1353 606:585-593.
1354 Sepulcri, C., C. Dentone, M. Mikulska, B. Bruzzone, A. Lai, D. Fenoglio, F. Bozzano, A. Bergna,
1355 A. Parodi, T. Altosole, E. Delfino, G. Bartalucci, A. Orsi, A. Di Biagio, G. Zehender, F.
1356 Ballerini, S. Bonora, A. Sette, R. De Palma, G. Silvestri, A. De Maria, and M. Bassetti.

2021. The Longest Persistence of Viable SARS-CoV-2 With Recurrence of Viremia and Relapsing Symptomatic COVID-19 in an Immunocompromised Patient-A Case Study. *Open Forum Infect Dis*. 8:ofab217.

Serrano-Lopez, J., S. Hegde, S. Kumar, J. Serrano, J. Fang, A.M. Wellendorf, P.A. Roche, Y. Rangel, L.J. Carrington, H. Geiger, H.L. Grimes, S. Luther, I. Maillard, J. Sanchez-Garcia, D.T. Starczynowski, and J.A. Cancelas. 2021. Inflammation rapidly recruits mammalian GMP and MDP from bone marrow into regional lymphatics. *Elife*. 10.

Shrestha, L.B., C. Foster, W. Rawlinson, N. Tedla, and R.A. Bull. 2022. Evolution of the SARS-CoV-2 omicron variants BA.1 to BA.5: Implications for immune escape and transmission. *Rev Med Virol*. 32:e2381.

Stephenson, E., G. Reynolds, R.A. Botting, F.J. Calero-Nieto, M.D. Morgan, Z.K. Tuong, K. Bach, W. Sungnak, K.B. Worlock, M. Yoshida, N. Kumasaka, K. Kania, J. Engelbert, B. Olabi, J.S. Spegarova, N.K. Wilson, N. Mende, L. Jardine, L.C.S. Gardner, I. Goh, D. Horsfall, J. McGrath, S. Webb, M.W. Mather, R.G.H. Lindeboom, E. Dann, N. Huang, K. Polanski, E. Prigmore, F. Gothe, J. Scott, R.P. Payne, K.F. Baker, A.T. Hanrath, I.C.D. Schim van der Loeff, A.S. Barr, A. Sanchez-Gonzalez, L. Bergamaschi, F. Mescia, J.L. Barnes, E. Kilich, A. de Wilton, A. Saigal, A. Saleh, S.M. Janes, C.M. Smith, N. Gopee, C. Wilson, P. Coupland, J.M. Coxhead, V.Y. Kiselev, S. van Dongen, J. Bacardit, H.W. King, I. Cambridge Institute of Therapeutic, C.-B.C. Infectious Disease-National Institute of Health Research, A.J. Rostron, A.J. Simpson, S. Hambleton, E. Laurenti, P.A. Lyons, K.B. Meyer, M.Z. Nikolic, C.J.A. Duncan, K.G.C. Smith, S.A. Teichmann, M.R. Clatworthy, J.C. Marioni, B. Gottgens, and M. Haniffa. 2021. Single-cell multi-omics analysis of the immune response in COVID-19. *Nat Med*. 27:904-916.

Sun, R., Z. Zhao, C. Fu, Y. Wang, Z. Guo, C. Zhang, L. Liu, C. Zhang, C. Shu, J. He, Y.G. Yang, S. Hua, Y. Gao, and Z. Hu. 2022a. Humanized mice for investigating SARS-CoV-2 lung infection and associated human immune responses. *Eur J Immunol*. 52:1640-1647.

Sun, X., A.K. Perl, R. Li, S.M. Bell, E. Sajti, V.V. Kalinichenko, T.V. Kalin, R.S. Misra, H. Deshmukh, G. Clair, J. Kyle, L.E. Crotty Alexander, J.A. Masso-Silva, J.A. Kitzmiller, K.A. Wikenheiser-Brokamp, G. Deutsch, M. Guo, Y. Du, M.P. Morley, M.J. Valdez, H.V. Yu, K. Jin, E.E. Bardes, J.A. Zepp, T. Neithamer, M.C. Basil, W.J. Zacharias, J. Verheyden, R. Young, G. Bandyopadhyay, S. Lin, C. Ansong, J. Adkins, N. Salomonis, B.J. Aronow, Y. Xu, G. Pryhuber, J. Whitsett, E.E. Morrisey, and N.L. Consortium. 2022b. A census of the lung: CellCards from LungMAP. *Dev Cell*. 57:112-145 e112.

Tveita, A., S.L. Murphy, J.C. Holter, A.B. Kildal, A.E. Michelsen, T.V. Lerum, M. Kaarbo, L. Heggelund, A.R. Holten, A.K. Finbraten, K.E. Muller, A. Mathiessen, S. Boe, B. Fevang, B.K. Granerud, K. Tonby, A. Lind, S.G. Dudman, K.N. Henriksen, F. Muller, O.H. Skjonsberg, M. Troseid, A. Barratt-Due, A.M. Dyrhol-Riise, P. Aukrust, B. Halvorsen, T.B. Dahl, T. Ueland, N.-S. Consortium, and S.-C.-S.G.I. the Norwegian. 2022. High Circulating Levels of the Homeostatic Chemokines CCL19 and CCL21 Predict Mortality and Disease Severity in COVID-19. *J Infect Dis*. 226:2150-2160.

Wahl, A., C. De, M. Abad Fernandez, E.M. Lenarcic, Y. Xu, A.S. Cockrell, R.A. Cleary, C.E. Johnson, N.J. Schramm, L.M. Rank, I.G. Newsome, H.A. Vincent, W. Sanders, C.R. Aguilera-Sandoval, A. Boone, W.H. Hildebrand, P.A. Dayton, R.S. Baric, R.J. Pickles, M. Braunstein, N.J. Moorman, N. Goonetilleke, and J. Victor Garcia. 2019. Precision mouse models with expanded tropism for human pathogens. *Nat Biotechnol*. 37:1163-1173.

Wahl, A., L. Gralinski, C. Johnson, W. Yao, M. Kovarova, K. Dinnon, H. Liu, V. Madden, H. Krzystek, C. De, K. White, A. Schafer, T. Zaman, S. Leist, P. Grant, K. Gully, F. Askin, E. Browne, C. Jones, R. Pickles, R. Baric, and J.V. Garcia. 2020. Acute SARS-CoV-2 Infection is Highly Cytopathic, Elicits a Robust Innate Immune Response and is Efficiently Prevented by EIDD-2801. *Res Sq*.

1407 Wahl, A., L.E. Gralinski, C.E. Johnson, W. Yao, M. Kovarova, K.H. Dinnon, 3rd, H. Liu, V.J.
1408 Madden, H.M. Krzystek, C. De, K.K. White, K. Gully, A. Schafer, T. Zaman, S.R. Leist,
1409 P.O. Grant, G.R. Bluemling, A.A. Kolykhalov, M.G. Natchus, F.B. Askin, G. Painter, E.P.
1410 Browne, C.D. Jones, R.J. Pickles, R.S. Baric, and J.V. Garcia. 2021. SARS-CoV-2
1411 infection is effectively treated and prevented by EIDD-2801. *Nature*. 591:451-457.
1412 Wauters, E., P. Van Mol, A.D. Garg, S. Jansen, Y. Van Herck, L. Vanderbeke, A. Bassez, B.
1413 Boeckx, B. Malengier-Devlies, A. Timmerman, T. Van Brussel, T. Van Buyten, R.
1414 Schepers, E. Heylen, D. Dauwe, C. Dooms, J. Gunst, G. Hermans, P. Meersseman, D.
1415 Testelmans, J. Yserbyt, S. Tejpar, W. De Wever, P. Matthys, J. Neyts, J. Wauters, J. Qian,
1416 and D. Lambrechts. 2021. Discriminating mild from critical COVID-19 by innate and
1417 adaptive immune single-cell profiling of bronchoalveolar lavages. *Cell Res*. 31:272-290.
1418 Wendisch, D., O. Dietrich, T. Mari, S. von Stillfried, I.L. Ibarra, M. Mittermaier, C. Mache, R.L.
1419 Chua, R. Knoll, S. Timm, S. Brumhard, T. Krammer, H. Zauber, A.L. Hiller, A. Pascual-
1420 Reguant, R. Mothes, R.D. Bulow, J. Schulze, A.M. Leipold, S. Djudjaj, F. Erhard, R.
1421 Geffers, F. Pott, J. Kazmierski, J. Radke, P. Pergantis, K. Bassler, C. Conrad, A.C.
1422 Aschenbrenner, B. Sawitzki, M. Landthaler, E. Wyler, D. Horst, C.-O.I. Deutsche, S.
1423 Hippenstiel, A. Hocke, F.L. Heppner, A. Uhrig, C. Garcia, F. Machleidt, S. Herold, S.
1424 Elezkurtaj, C. Thibeault, M. Witzenrath, C. Cochain, N. Suttorp, C. Drosten, C. Goffinet,
1425 F. Kurth, J.L. Schultze, H. Radbruch, M. Ochs, R. Eils, H. Muller-Redetzky, A.E. Hauser,
1426 M.D. Luecken, F.J. Theis, C. Conrad, T. Wolff, P. Boor, M. Selbach, A.E. Saliba, and L.E.
1427 Sander. 2021. SARS-CoV-2 infection triggers profibrotic macrophage responses and lung
1428 fibrosis. *Cell*. 184:6243-6261 e6227.
1429 Xu, S.W., I. Ilyas, and J.P. Weng. 2023. Endothelial dysfunction in COVID-19: an overview of
1430 evidence, biomarkers, mechanisms and potential therapies. *Acta Pharmacol Sin*. 44:695-
1431 709.
1432 Yan, Y., R. Chen, X. Wang, K. Hu, L. Huang, M. Lu, and Q. Hu. 2019. CCL19 and CCR7
1433 Expression, Signaling Pathways, and Adjuvant Functions in Viral Infection and Prevention.
1434 *Front Cell Dev Biol*. 7:212.
1435 Yang, D., H. Chu, Y. Hou, Y. Chai, H. Shuai, A.C. Lee, X. Zhang, Y. Wang, B. Hu, X. Huang, T.T.
1436 Yuen, J.P. Cai, J. Zhou, S. Yuan, A.J. Zhang, J.F. Chan, and K.Y. Yuen. 2020. Attenuated
1437 Interferon and Proinflammatory Response in SARS-CoV-2-Infected Human Dendritic
1438 Cells Is Associated With Viral Antagonism of STAT1 Phosphorylation. *J Infect Dis*.
1439 222:734-745.
1440 Yoo, J.S., M. Sasaki, S.X. Cho, Y. Kasuga, B. Zhu, R. Ouda, Y. Orba, P. de Figueiredo, H. Sawa,
1441 and K.S. Kobayashi. 2021. SARS-CoV-2 inhibits induction of the MHC class I pathway by
1442 targeting the STAT1-IRF1-NLRC5 axis. *Nat Commun*. 12:6602.
1443 Zhang, Y., Y. Chen, and Z. Meng. 2020. Immunomodulation for Severe COVID-19 Pneumonia:
1444 The State of the Art. *Frontiers in Immunology*. 11.
1445 Zheng, J., Y. Wang, K. Li, D.K. Meyerholz, C. Allamargot, and S. Perlman. 2021. Severe Acute
1446 Respiratory Syndrome Coronavirus 2-Induced Immune Activation and Death of Monocyte-
1447 Derived Human Macrophages and Dendritic Cells. *J Infect Dis*. 223:785-795.

1448

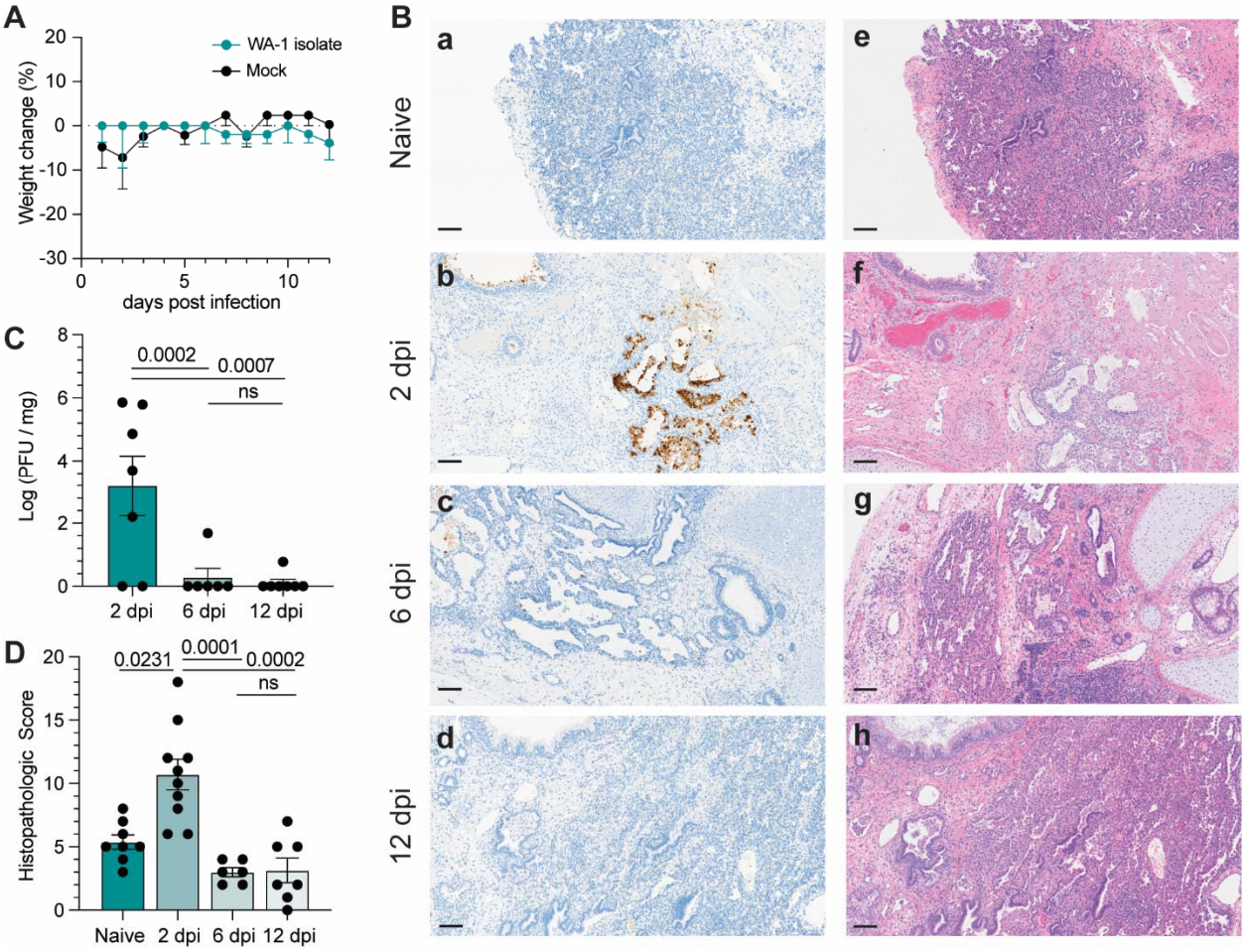
A
WA-1 isolate
Mock
Weight change (%)
days post infection
B
Naive
2 dpi
6 dpi
12 dpi
a
b
c
d
e
f
g
h
C
Log (PFU / mg)
0.0002
0.0007
ns
2 dpi
6 dpi
12 dpi
D
Histopathologic Score
0.0231
0.0001
0.0002
ns
Naive
2 dpi
6 dpi
12 dpi

Figure 1

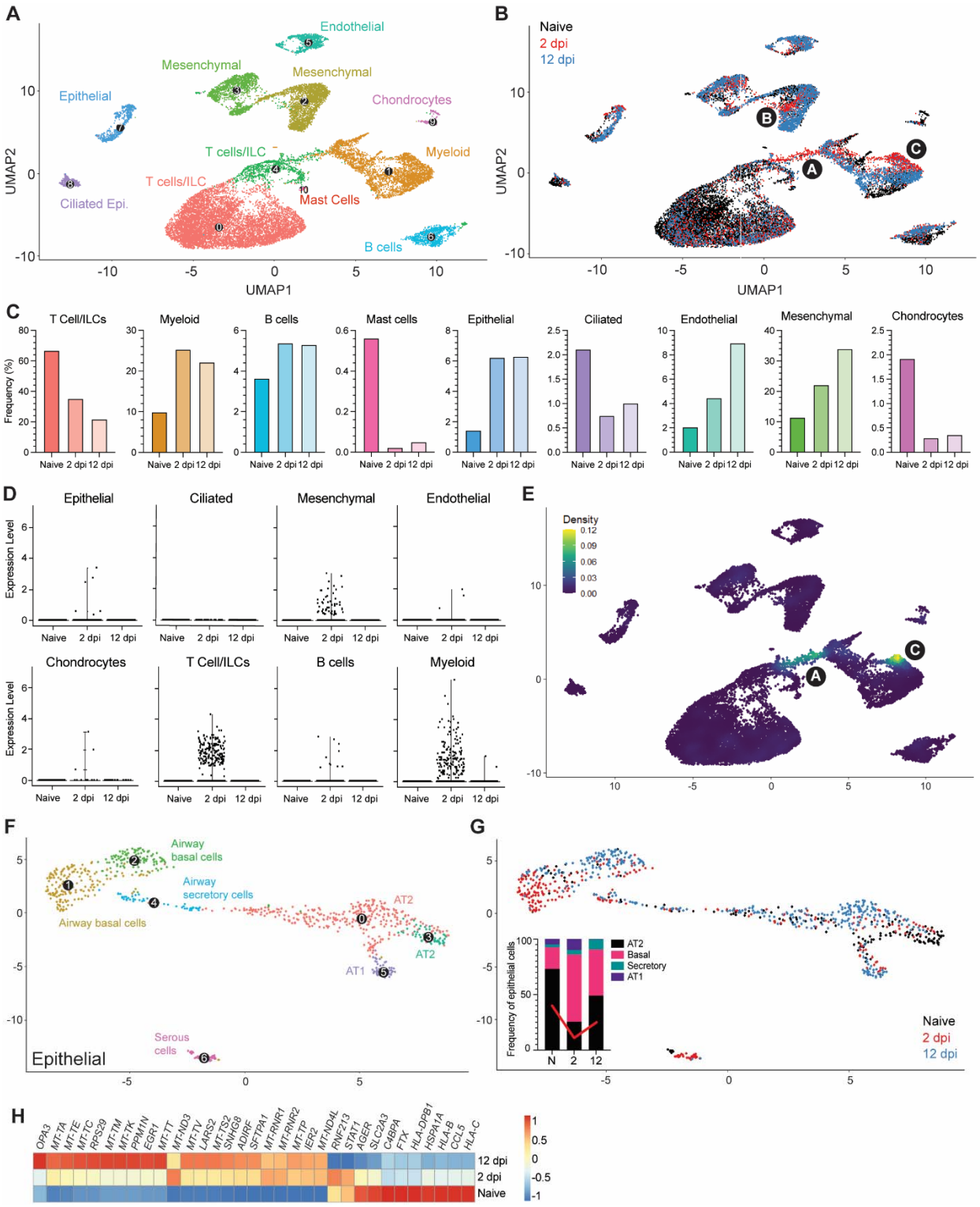
A
Endothelial
Mesenchymal
Mesenchymal
Epithelial
Chondrocytes
T cells/ILC
Myeloid
T cells/ILC
Mast Cells
Ciliated Epi.
B cells
UMAP2
UMAP1
B
Naive
2 dpi
12 dpi
C
T Cell/ILCs
Myeloid
B cells
Mast cells
Epithelial
Ciliated
Endothelial
Mesenchymal
Chondrocytes
Frequency (%)
Naive 2 dpi 12 dpi
D
Epithelial
Ciliated
Mesenchymal
Endothelial
Chondrocytes
T Cell/ILCs
B cells
Myeloid
Expression Level
E
Density
F
Airway basal cells
Airway secretory cells
Airway basal cells
AT2
AT2
AT1
Serous cells
Epithelial
G
Frequency of epithelial cells
AT2
Basal
Secretory
AT1
N 2 12
Naive
2 dpi
12 dpi
H
OPA3 MT-TA MT-TE MT-TC RPS29 MT-TM MT-TK PPM1N EGR1 MT-TT MT-ND3 MT-TV LARS2 MT-TS2 SNHG8 ADIRF SFTPA1 MT-RNR1 MT-RNR2 MT-TP IER2 MT-ND4L RNF213 STAT1 AGER SLC2A3 C4BPA FTX HLA-DPB1 HSPA1A HLA-B CCL5 HLA-C
12 dpi
2 dpi
Naive

Figure 2

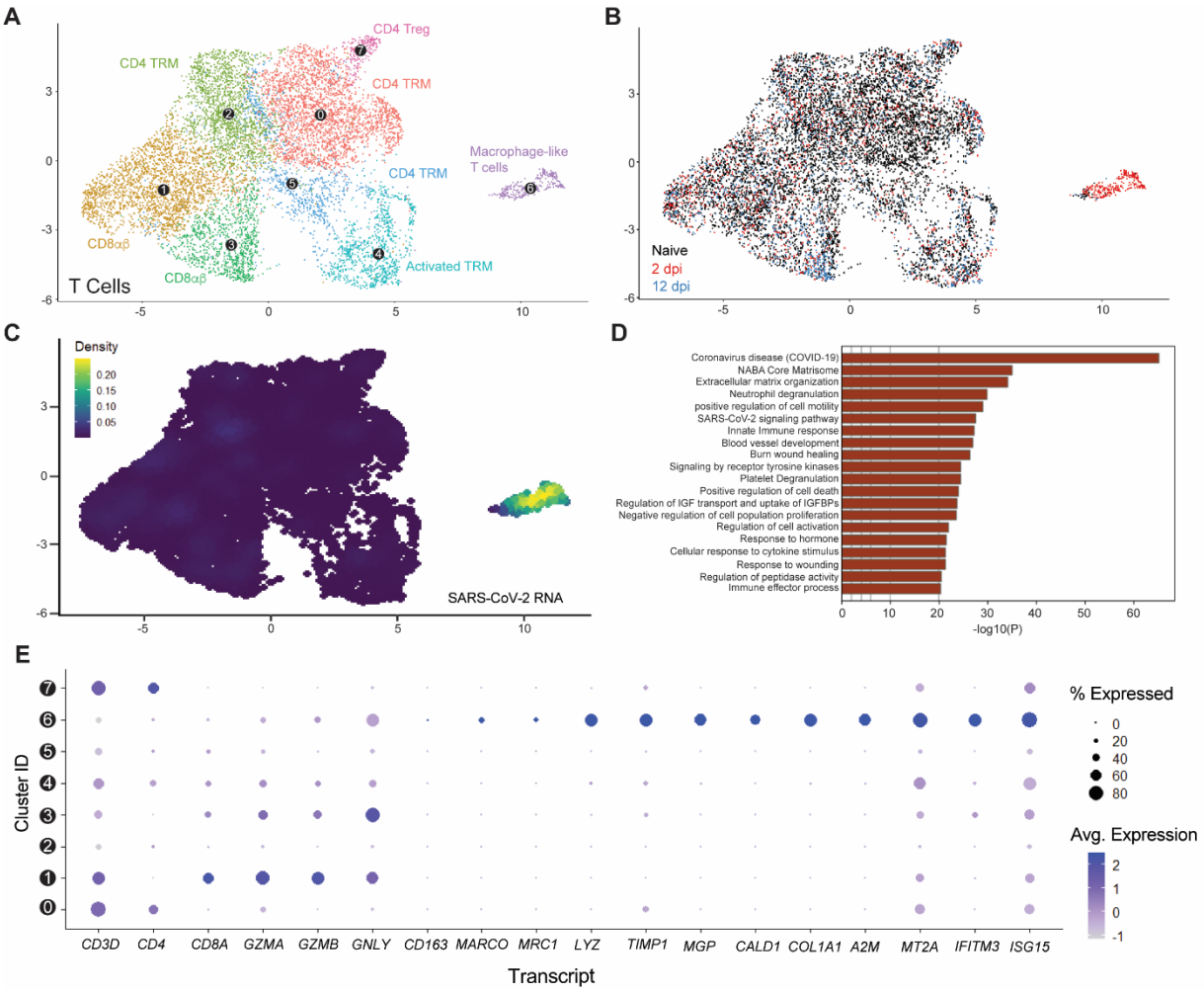
A
CD4 Treg
CD4 TRM
CD4 TRM
CD4 TRM
Macrophage-like T cells
CD8αβ
CD8αβ
Activated TRM
T Cells
B
Naive
2 dpi
12 dpi
C
Density
0.20
0.15
0.10
0.05
SARS-CoV-2 RNA
D
Coronavirus disease (COVID-19)
NABA Core Matrisome
Extracellular matrix organization
Neutrophil degranulation
positive regulation of cell motility
SARS-CoV-2 signaling pathway
Innate Immune response
Blood vessel development
Burn wound healing
Signaling by receptor tyrosine kinases
Platelet Degranulation
Positive regulation of cell death
Regulation of IGF transport and uptake of IGFBPs
Negative regulation of cell population proliferation
Regulation of cell activation
Response to hormone
Cellular response to cytokine stimulus
Response to wounding
Regulation of peptidase activity
Immune effector process
-log10(P)
E
Cluster ID
CD3D
CD4
CD8A
GZMA
GZMB
GNLY
CD163
MARCO
MRC1
LYZ
TIMP1
MGP
CALD1
COL1A1
A2M
MT2A
IFITM3
ISG15
Transcript
% Expressed
Avg. Expression

Figure 3

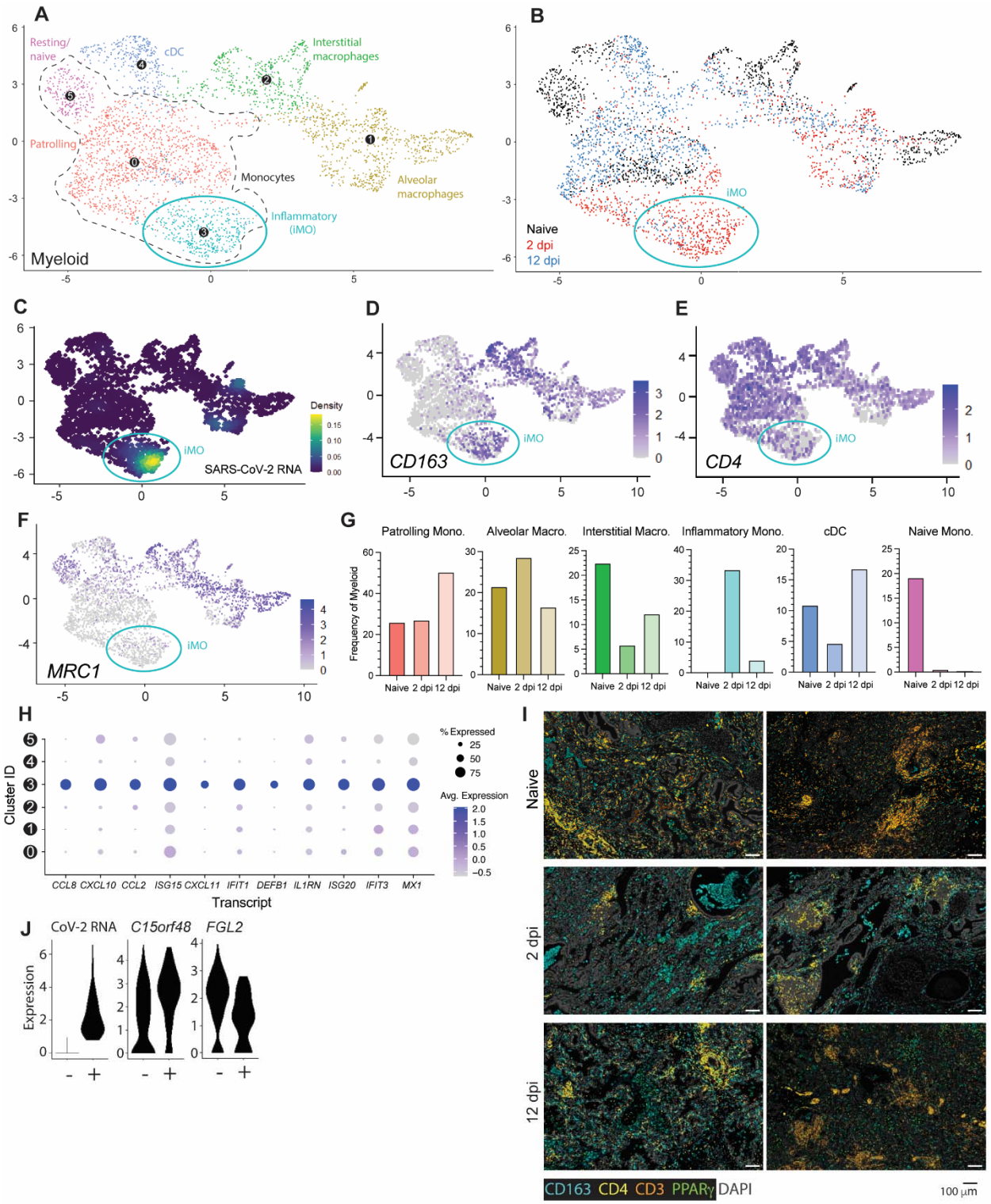
A
Resting/ naive
cDC
Interstitial macrophages
Patrolling
Monocytes
Alveolar macrophages
Inflammatory (iMO)
Myeloid
B
iMO
Naive
2 dpi
12 dpi
C
Density
iMO
SARS-CoV-2 RNA
D
iMO
CD163
E
iMO
CD4
F
iMO
MRC1
G
Patrolling Mono.
Alveolar Macro.
Interstitial Macro.
Inflammatory Mono.
cDC
Naive Mono.
Frequency of Myeloid
Naive 2 dpi 12 dpi
H
Cluster ID
% Expressed
Avg. Expression
CCL8 CXCL10 CCL2 ISG15 CXCL11 IFIT1 DEFB1 IL1RN ISG20 IFIT3 MX1
Transcript
I
Naive
2 dpi
12 dpi
CD163 CD4 CD3 PPARγ DAPI
100 μm
J
CoV-2 RNA
C15orf48
FGL2
Expression
- +

Figure 4

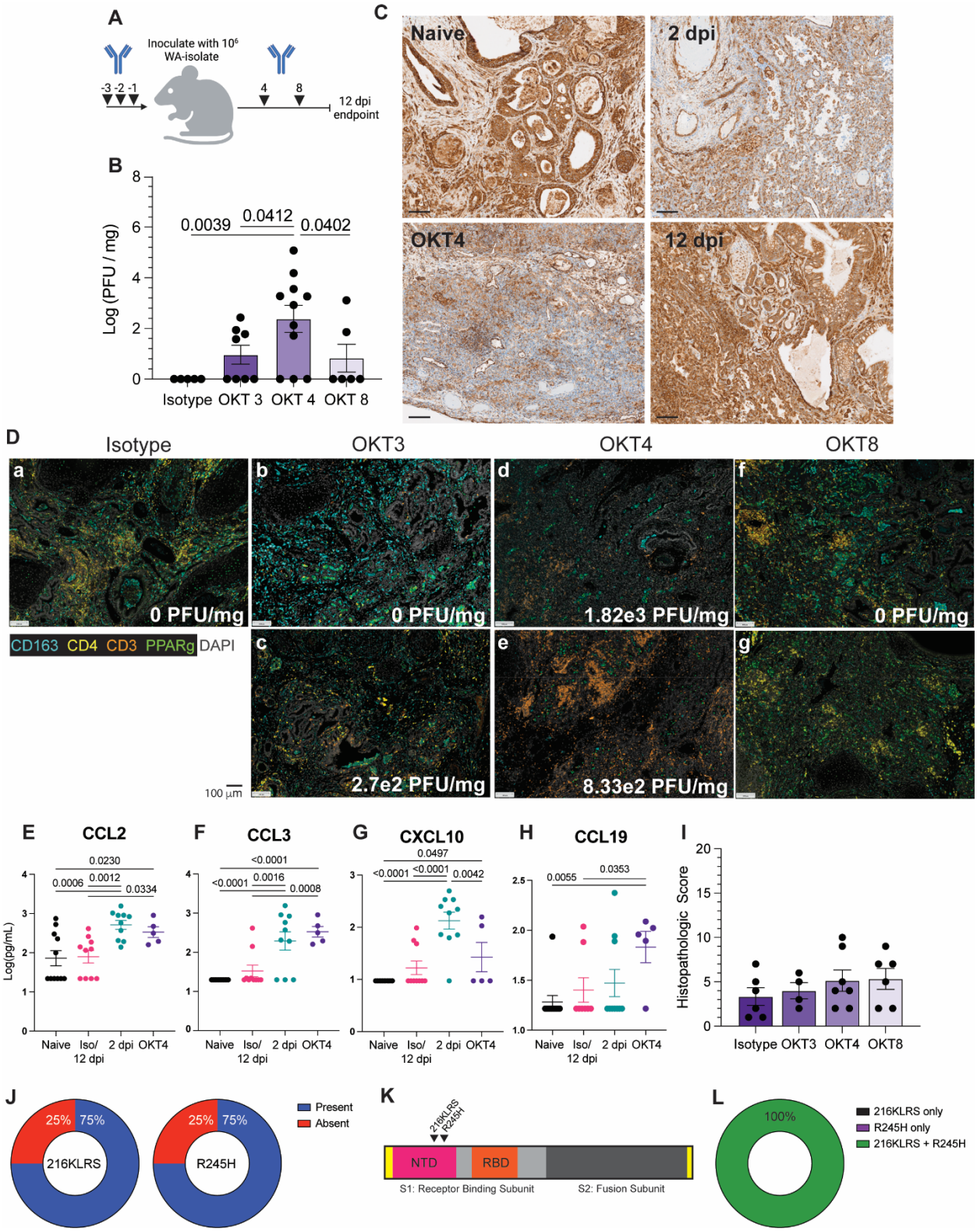
A
Inoculate with 10⁶ WA-isolate
-3 -2 -1
4
8
12 dpi endpoint
B
Log (PFU / mg)
0.0039
0.0412
0.0402
Isotype OKT 3 OKT 4 OKT 8
C
Naive
2 dpi
OKT4
12 dpi
D
Isotype
OKT3
OKT4
OKT8
0 PFU/mg
0 PFU/mg
1.82e3 PFU/mg
0 PFU/mg
CD163 CD4 CD3 PPARg DAPI
2.7e2 PFU/mg
8.33e2 PFU/mg
100 µm
E CCL2
F CCL3
G CXCL10
H CCL19
I
Log(pg/mL)
Naive Iso/ 12 dpi 2 dpi OKT4
Histopathologic Score
Isotype OKT3 OKT4 OKT8
J
25% 75%
216KLRS
R245H
Present
Absent
K
216KLRS
R245H
NTD
RBD
S1: Receptor Binding Subunit
S2: Fusion Subunit
L
100%
216KLRS only
R245H only
216KLRS + R245H

Figure 5

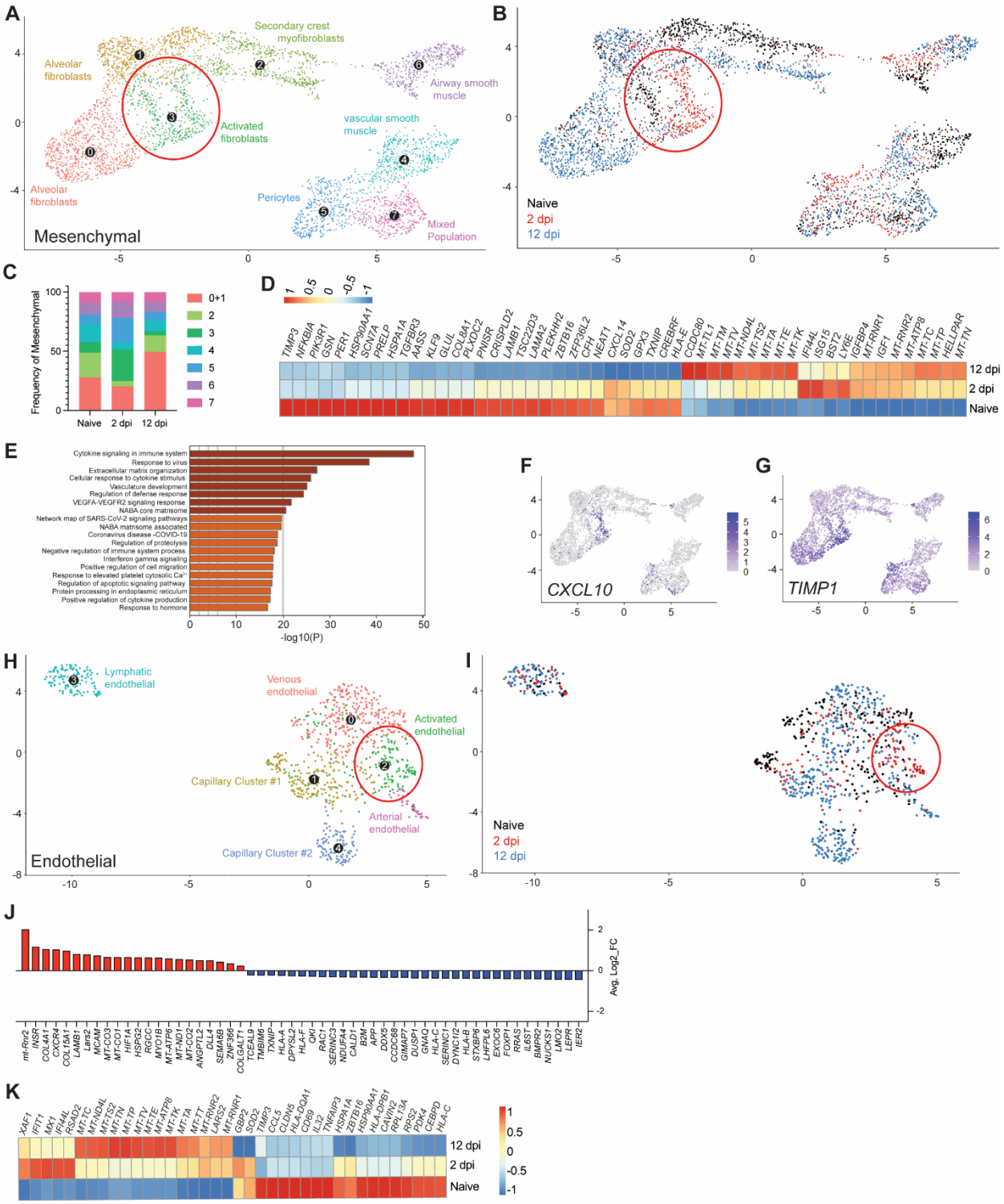
A
Alveolar fibroblasts
Secondary crest myofibroblasts
Airway smooth muscle
Activated fibroblasts
vascular smooth muscle
Alveolar fibroblasts
Pericytes
Mixed Population
Mesenchymal
B
Naive
2 dpi
12 dpi
C
Frequency of Mesenchymal
Naive
2 dpi
12 dpi
D
12 dpi
2 dpi
Naive
E
-log10(P)
F
CXCL10
G
TIMP1
H
Lymphatic endothelial
Venous endothelial
Activated endothelial
Capillary Cluster #1
Arterial endothelial
Capillary Cluster #2
Endothelial
I
Naive
2 dpi
12 dpi
J
Avg. Log2_FC
K
12 dpi
2 dpi
Naive

Figure 6

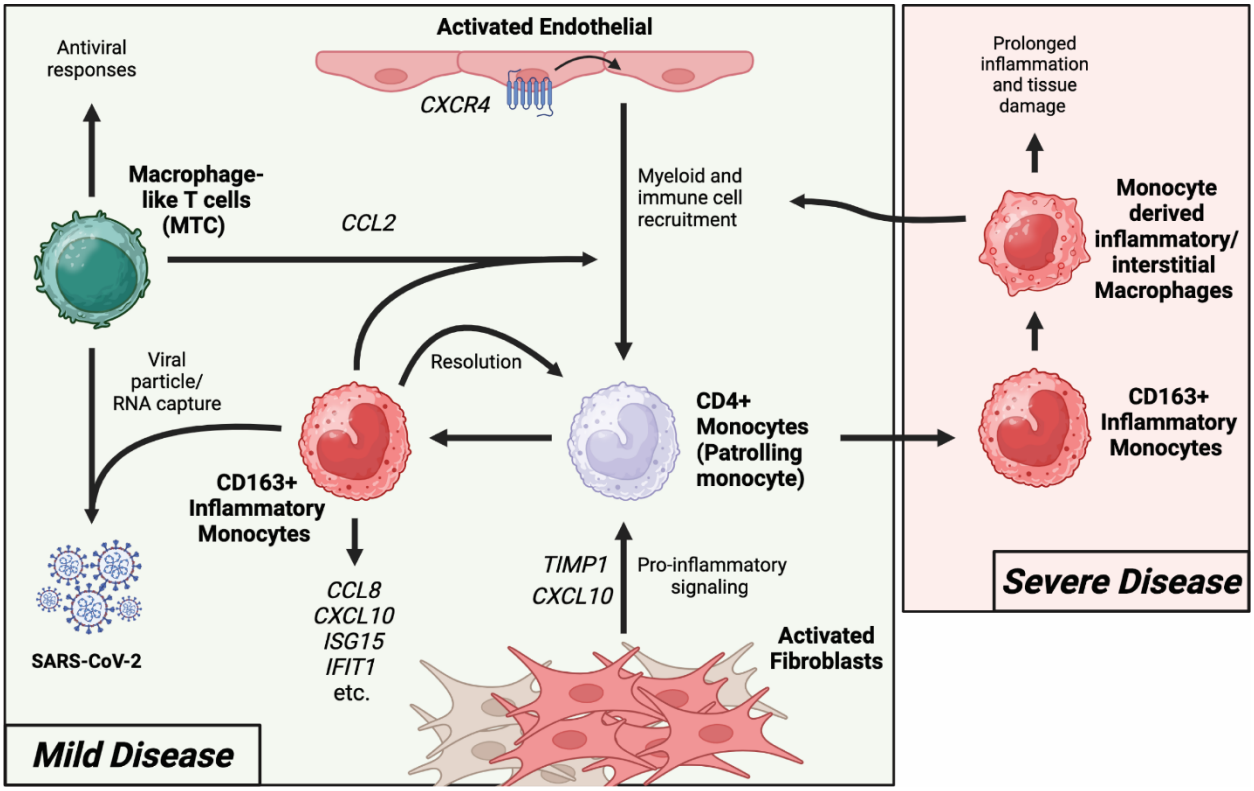
Activated Endothelial
CXCR4
Antiviral responses
Macrophage-like T cells (MTC)
CCL2
Myeloid and immune cell recruitment
Viral particle/ RNA capture
Resolution
CD163+ Inflammatory Monocytes
CD4+ Monocytes (Patrolling monocyte)
SARS-CoV-2
CCL8
CXCL10
ISG15
IFIT1
etc.
TIMP1
CXCL10
Pro-inflammatory signaling
Activated Fibroblasts
Mild Disease
Prolonged inflammation and tissue damage
Monocyte derived inflammatory/ interstitial Macrophages
CD163+ Inflammatory Monocytes
Severe Disease

Figure 7